Successive stages and the role of natural vortex dislocations in three-dimensional wake transition

By M. BRAZA,[1] D. FAGHANI[2] AND H. PERSILLON[1]

[1]IMFT-Unité Mixte de Recherche CNRS-INPT 5502, Avenue du Prof. C. Soula,
31400 Toulouse, France

[2]EAI Tech, CERAM Sophia-Antipolis, 157, rue A. Einstein, BP 085,
06902 Sophia-Antipolis Cedex, France

The time-history of the development of the three-dimensional transition features in a nominally two-dimensional flow configuration is established for Reynolds number 220 in a cylinder wake. The identification of the successive stages that evolve very fast during experiments is possible by means of direct numerical simulation. The physical processes related to the creation of streamwise and vertical vorticity components and their impact on the spanwise waviness of the main von Kármán vortex filaments are analysed by means of the Craik–Leibovich shearing instability mechanism and a comparative discussion is given with respect to the elliptic stability theory. This study proves the existence of a further stage in the three-dimensional transition, which substantially modifies the regular spanwise undulation. This is a systematic and repetitive development of natural vortex dislocations in the near wake. The definition of this kind of structure is provided, as well as its properties related to a drastic reduction of the fundamental frequency and to the selection of a lower path in the Strouhal–Reynolds number relation. The induced amplitude modulation of the flow properties along the span is also evaluated. Quantification of these properties is carried out by using *wavelet* analysis and autoregressive modelling of the time series. The reasons for the development of natural vortex dislocations are analysed and related to specific modulations of the spanwise structure of the longitudinal velocity upstream separation. From this part of the study an optimum shape for the spanwise distribution of this component can be specified, able to trigger the vortex dislocations in wake flows and therefore useful to apply in the context of stability theory analyses and in further DNS studies.

1. Introduction

The transition to turbulence in the wake of bluff bodies has been the objective of a considerable number of studies over the whole of the last century from both an experimental and numerical point of view. In the last decade, owing to advanced experimental methodologies for velocity field measurements and flow visualizations, an ensemble of complex physical phenomena related to the three-dimensional transition has been studied in this category of flows and has contributed to a better understanding of the flow patterns observed since the 1950s. Simultaneously, due to the increased capabilities of supercomputers, a smaller number of numerical investigations of the three-dimensional transition for the same category of flows has

appeared, based on direct numerical simulation (DNS). In a previous work of ours (Persillon & Braza 1998*b*) a summary of transition features investigated numerically and on the basis of experiments was reported. A comprehensive discussion on experimentally investigated wake transition phenomena is given by Williamson (1996). Although since the 1980s the advances in numerical methodologies have allowed simulation of three-dimensional separation and of complex unsteady vortex structures in flows with simple configurations (flat-plate boundary layer, free shear layers, jets, ...), there are many fewer three-dimensional direct simulations of flows past bluff bodies. This is due to difficulties arising from the simultaneous presence of the non-rectilinear form of the solid wall and of the unbounded, non-confined character of these flows, therefore requiring an extremely high number of degrees of freedom to obtain the complete established phase of these kinds of transition features. The study of Thompson, Hourigan & Sheridan (1994) was among the first to simulate the onset of spanwise undulations as a first step to three-dimensional transition in the flow past a circular cylinder. The same features, as well as the simulation of the first discontinuity frequency drop, were obtained by Zhang *et al.* (1996) and by Mittal & Balachandar (1995). Persillon, Braza & Jin (1995) simulated the formation of the discontinuity region in the Strouhal–Reynolds number (*St*, *Re*) relation, delimited by two frequency steps in the Reynolds number range 180–300, and the same research team has quantified the discontinuous kinetic energy distribution within the same Reynolds number range, contributing to the explanation of the formation of this transition feature.

Simultaneously with these studies attempting to simulate directly these phenomena by using the complete Navier–Stokes equations, methods based on linear stability theory have been able to determine the creation of mode A undulation by perturbing the two-dimensional vortex pattern obtained by two-dimensional Navier–Stokes simulations. These studies have quantified the expected wavelength and the critical Reynolds number for its appearance (Barkley & Henderson 1996) by using Floquet-type spanwise perturbations of the linearized equations of motion. In their study, the subcritical nature of the secondary instability related to mode A was proved by considering a discretized form of the Stuart–Landau equation. As their linear Floquet stability analysis takes into account the influence of infinitesimal perturbations, it is expected that the critical Reynolds number evaluated is slightly higher than in the physical reality. Indeed, the additional influence of finite-amplitude perturbations, inherent to the alternating nature of the vortex shedding, is decisive in creating the first discontinuity in the *St*, *Re* relation as an abrupt step. In this sense, the approach using the three-dimensional Navier–Stokes equations offered the possibility of taking into account these effects and quantifying the critical Reynolds number for the first discontinuity at a lower value ($Re = 187$) than that predicted by the linear theory (Persillon & Braza 1998*b*).

This study has also evaluated the spanwise wavelength shortening that occurs as the Reynolds number further increases in the range 240–260, related to mode B waviness.

However, even with the current capabilities of supercomputers, the evaluation of this critical Reynolds number value remains a non-trivial task, needing a considerable number of three-dimensional time-dependent simulations. For these reasons, the linear stability theories remain an interesting approach for a first assessment of critical parameters in three-dimensional transition using reasonable CPU times. In the same context of linear Floquet theory, Henderson (1997) has reported that mode B is a supercritical bifurcation and has determined the critical Reynolds number for this

change. The same study provided direct Navier–Stokes simulations for Reynolds numbers in the vicinity of the mode B range and also at Reynolds number 1000.

The amplification of the instability process and its spatial properties can indeed be evaluated by the Navier–Stokes approach, through the evolution of the maximum spectral amplitude of the vortex shedding motion. This strategy, following experimental studies of global modes in wakes by Goujon-Durand, Jenffer & Wesfreid (1994) has been adopted in the study by Persillon & Braza (1998b) and has provided the mapping and the variation laws of the amplification process of the von Kármán instability along the rear axis as a function of Reynolds number, by means of direct three-dimensional simulation. However, the amplitude variations along the spanwise direction, due to the secondary instability, have not yet been assessed. This is one of the objectives of the present study.

Beyond the spanwise undulations discussed above, which provide quasi-periodic spanwise variations of the velocity signals, earlier experimental works by Roshko (1954) reports the existence of a transition regime for the wake past the cylinder, where he found distinct irregularities in the wake velocity fluctuations. It was suggested later by Bloor (1964) that the low-frequency irregularities measured in the wake are linked to three-dimensional motion that would progressively contaminate the downstream flow and produce turbulent motion. This more chaotic behaviour of the motion may be linked to further transition features other than the spanwise modes. A main objective of the present paper is to analyse the existence of additional transition features which would modify the spanwise undulated structure as a systematic route to turbulence, and would be associated with the observed irregular character of the flow.

In the case of free shear flows, the vortex rows shed downstream may form cells of different frequency as has been experimentally obtained by Browand & Troutt (1980, 1985). Due to this kind of irregularity, the vortex rows lose locally their continuity and develop 'vortex defects' or vortex dislocations, which appear naturally in the flow. This kind of structure may have a systematic appearance and lead to formation of a 'treillis' structure as has been recently shown by field measurements using hot-wire combs (Vincendeau 1995) and by direct and large-eddy simulations of forced mixing layers (Lesieur, Comte & Métais 1995). Concerning bluff body wakes, natural vortex dislocations have been obtained experimentally in flows past cones, where the geometric variation of the diameter locally creates a variation of the Strouhal number along the span (Gaster 1969). A remarkably good agreement with the cells formed has been obtained by the numerical simulations of Jesperson & Levit (1991) for this kind of wake flow.

For the cylinder wake, Williamson (1992) discovered the existence of 'spot-like', natural vortex dislocations and related them to velocity fluctuations in the near wake. In order to provide a more regular and systematic appearance of their dynamic characteristics, a considerable part of that study was devoted to the investigation of forced vortex dislocations triggered by a ring at the cylinder median section. Therefore, apart from that first study showing the existence of natural vortex dislocations, the appearance of this kind of structure as a systematic transition feature remains an open question in bluff body wakes. Moreover, only very few attempts to analyse this kind of structure as an inherent transition feature by direct numerical simulation exist, due to very severe requirements in spanwise length and number of grid points needed. In this context, Persillon, Braza & Williamson (1997) and Persillon & Braza (1998a) have shown that vortex dislocations are spontaneously formed in the near wake of a circular cylinder in the Reynolds number range corresponding to a clearly

obtained development of mode A and the detected structures have been found in good qualitative agreement with the experiment. That study is a starting point for the present one. There is still a poor understanding of the main dynamic properties characterizing and qualifying a modification of the spanwise vortex structure as a natural vortex dislocation and the reasons for the appearance of this kind of structure are not yet thoroughly known. Furthermore, the impact of vortex dislocations on the creation of different kinds of fluctuations related to the inception of turbulent motion needs to be quantified, in order to establish a precise scenario of the transition to turbulence in bluff body wakes and to examine whether natural vortex dislocations constitute a successive step of transition, modifying the spanwise undulation. In view of this discussion, the objectives of the present paper are summarized as follows:

(i) Analyse the inherent way that three-dimensionality is established in the flow around the cylinder, departing from the initial stage of a two-dimensional flow beyond the first bifurcation and governed by the alternating von Kármán vortex pattern. This study aims at a clear identification of the scenario of the first steps in the three-dimensional transition in bluff body wakes.

(ii) Study the mechanisms responsible for the spontaneous creation of organized spanwise undulations on the originally rectilinear alternating vortex rows. Explain the formation of the expected modes by means of different stability theory considerations.

(iii) Track the existence of further inherent modifications of the undulated vortex rows by a detailed investigation of the three-dimensional vorticity and velocity fields. In particular, the existence of a regular appearance of natural vortex dislocations is investigated.

(iv) Examine the reasons and main physical mechanisms responsible for the development of natural vortex dislocations; in particular, suggest the nature of perturbing factors typically able to trigger the natural vortex dislocations pattern as a systematic way of transition to turbulence.

The strategy chosen to achieve these objectives is the physical analysis of time and space signals of key quantities (vorticity and velocity components and pressure) obtained by direct numerical simulation of the flow past a circular cylinder of 'infinite' span (e.g. without using end plates). From a computational point of view, the rather high spanwise length of $12D$ is considered (in respect of CPU needs for a direct simulation), allowing investigation of these phenomena. The value of 220 chosen for the Reynolds number falls well within the range where mode A instability is fully developed.

Section 2 refers briefly to the governing equations and outlines the numerical method. Section 3 analyses the onset of three-dimensionality, a prerequisite step for the three-dimensional transition, preceding further modifications due to the vortex dislocations. A critical discussion on the fundamental mechanisms governing the spanwise undulation is provided, as well as the evaluation of the related wavelength, by using a long spanwise dimension compared with the previous studies. An assessment of this transition feature is also provided by means of stability theory considerations. A comparative discussion and synthesis based on these different approaches is given. Section 4 examines the natural vortex dislocation pattern by presenting the time-dependent evolution of vorticity fields along with some flow visualization. A definition of this kind of structure is provided, as well as its impact on the transition process. Subsection 4.1, entitled 'time–frequency analysis' is devoted to a detailed quantification of the different properties related to the vortex dislocations. Subsection 4.2 analyses upstream spanwise mechanisms related to causes of natural vortex dislocation formation in the near wake. Section 5 presents the conclusions of this study.

2. Theoretical formulation and numerical method

The governing equations for the flow of an incompressible viscous fluid past a circular cylinder are the continuity and the Navier–Stokes equations. The equations are written in a general curvilinear coordinate system normalized by the cylinder diameter D and the uniform upstream velocity. A detailed presentation of these equations and of the numerical method can be found in Persillon & Braza (1998*b*). The governing equations are written in general curvilinear coordinates in the (x, y)-plane while the z-component (in the spanwise direction) is in Cartesian coordinates.

The numerical method is based on the full three-dimensional Navier–Stokes equations for an incompressible fluid. The numerical procedure is summarized as follows. The pressure–velocity formulation is used along with a predictor–corrector pressure scheme similar to the one reported by Amsden & Harlow (1970) but extended to the case of an implicit formulation (Braza, chassaing & Ha Minh 1986). The temporal discretization is done by adopting the Douglas (1962) fractional scheme in an alternating direction implicit formulation. The boundary conditions are those specified in Persillon & Braza (1998*b*). At the spanwise free edges of the computational domain, periodic boundary conditions are applied. A comparison of Neumann type boundary conditions and of periodic ones with respect to their ability in simulating the development of three-dimensionality and of spanwise undulations has been performed in a number of our studies and proved their equal validity (Persillon & Braza 1998*a*; Bouhadji & Braza 1998). Another useful element of the present numerical method is the three-dimensional extension of non-reflecting type boundary conditions, based on the work by Jin & Braza (1987) in two dimensions.

In the following sections the results are discussed according to the phenomenology of the different classes of vortex structures obtained by the direct simulation and shown by contour plots of flow quantities, in qualitative comparison with Williamson (1992). The way that the three-dimensional motion is progressively established in the flow system is analysed. The numerical parameters were carefully chosen in a previous study of ours (Persillon & Braza 1998*b*). The grid sizes are $(150 \times 80 \times 62)$ to $(160 \times 100 \times 100)$. The numerical simulations are carried out for a rather long spanwise length value ($12D$) and several comparisons are done with a small spanwise length of $3.75D$: figures 3*a* and 5*a*, 3*b* and 5*b*, 3*c* and 5*c* corresponding to the small and large spanwise lengths. It is shown that the same kind of spanwise undulation and of streamwise vortex structures develop (as detailed in §3) in both cases. These results ensure that the studies with the two aspect ratios give similar results. In the field representations of the different contours of flow quantities, a dimensionless shift of 185 has to be added to the displayed time values, in order to obtain correspondence with the time values in §4.1.

3. The successive steps to three-dimensionality from a nominally two-dimensional flow configuration

One of the main themes of the present study is to understand how three-dimensional structures develop from nominally two-dimensional wake flows. Direct numerical simulation offers the possibility of studying these stages by examining the flow history from the beginning of the computation, to beyond the first two-dimensional bifurcation, whereas these steps evolve very fast in a physical experiment. The initial conditions are those of an established two-dimensional flow with vortex shedding providing a rectilinear configuration of alternating vortex rows along the span. During

the simulation, the way the flow progressively loses its two-dimensional character will be studied using the small numerical and truncation errors that play the role of small perturbations unavoidably existing in any physical experiment. In addition, a perturbation on the w velocity component constituting a white noise of order $10^{-4}U_{upstream}$ is applied in the inlet section of the computational domain in order to shorten the transient phase of the simulation. This order of magnitude is even less than the smallest turbulent intensity of the inlet section of wind tunnel experiments, including those of reference in the present study. Similar results have been obtained with a different amplitude level of white noise, still very small, of order $10^{-3}U_{upstream}$, concerning the onset of the secondary instability and the organization of w in coherent cells along the span. Therefore, as long as the imposed perturbations are small, the evolution of the flow system is independent of the perturbation and shows only inherent characteristics. Moreover, very long computations have also been performed without any perturbation in w. Again, the flow develops the three-dimensional effects and mode A development, but after a much longer transient phase, as was described in Persillon & Braza (1998b). In this case, the truncation and round-off errors played the role of perturbing factors to the flow system, which follows the same route to three-dimensional transition although their (random) distribution is different along the span. In the present study, random distributions for the w component are chosen, because otherwise preferential amplification or damping of specific three-dimensional modes would occur. That is not the objective of the present study, which focuses on inherent characteristics. Choosing specific distributions (non-random) of w concerning the amplitude and wavelength along the span would be a very interesting future way to study the forcing of secondary instability and bypass transition.

After a long transient phase during which the flow remains two-dimensional, the w velocity component (in the spanwise direction) progressively increases. The first stages of this evolution are proven to obey a linear growth up to dimensionless time value 150, as is shown in the $\log(A)$ versus period evolution (figure 1a), A being the amplitude of w oscillations, followed by the nonlinear phase. Soon after, this component starts to be organized into distinct cells, figure 1(b). As is expected from the continuity equation for an incompressible fluid, this pattern is followed by the appearance of organized counter-rotating cells of the streamwise vorticity component ω_x along the span, shown at time $t = 780$ in figure 2. The birth of streamwise vorticity is due to the progressive development of the w component as Reynolds number increases, owing to the influence of the small perturbations mentioned before. Under the action of the progressive increase of the streamwise vorticity, the two-dimensional main alternating vortices display a weak regular spanwise undulation. A perspective view of this initial three-dimensional modification of the originally rectilinear alternating vortices is shown in figure 3. The birth of this configuration is directly related to the amplification of the w component fluctuations and of the streamwise vorticity, interacting with the von Kármán vortex rows in a similar way to the mechanism identified for the spanwise undulation of vortices past a splitter plate by Lasheras & Meiburg (1990). In their study, the birth of streamwise vortex filaments was a result of cross-stream perturbations interacting with the main vortex rows which become undulated. This pattern was called mode 1. In the wake past a circular cylinder, this fundamental spanwise modification was discovered by Williamson (1992) and was called mode A. The present DNS precisely reveals the successive stages undergone by the flow transition prior to the establishment of the spanwise undulation.

It appears that this spanwise undulation is a general phenomenon characterizing the first steps of the three-dimensional transition in a wide range of wakes, as has
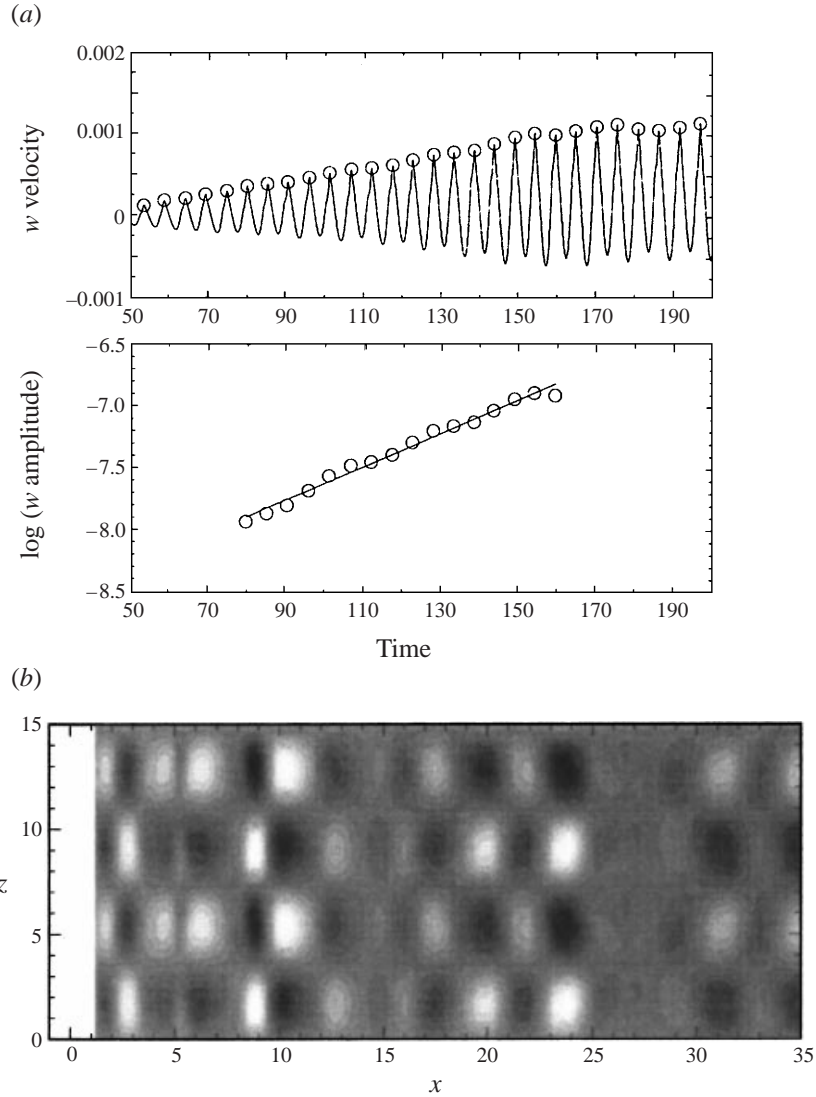
(*a*)

(*b*)

FIGURE 1. (*a*) Time evolution of the *w* velocity component, $(x/D, y/D, z/D = 1.4, 0, 1.0)$ (top); log[amplitude(*w*)] (bottom). (*b*) Iso-contours of the *w* velocity component at the initial stages of the flow, $t = 280$, $Re = 220$. (Two spanwise lengths are joined for a better visibility of the structures.)

been shown by our recent direct simulations of flows past wings at high incidence in incompressible regime (Hoarau *et al.* 2000) and also in the compressible (transonic) regime by Bouhadji & Braza (1998). In the present incompressible flow past the cylinder, at higher time values the streamwise vortices become more pronounced and inception of them occurs between two main alternating eddies in the formation region (figure 4). Then, the streamwise vortices travel downstream and progressively migrate towards the wake shear layer, in the convection region. Figure 5(*a–c*) shows the history of these stages related to the streamwise vortices formation and to the progressive development of mode A. It is found that the strength of the spanwise undulation increases from time $t = 680$ to $t = 740$ with the simultaneous increase of streamwise vorticity that forms progressively counter-rotating 'braid' like structures (see pairs of red and yellow vortices in figure 5*a–d*).
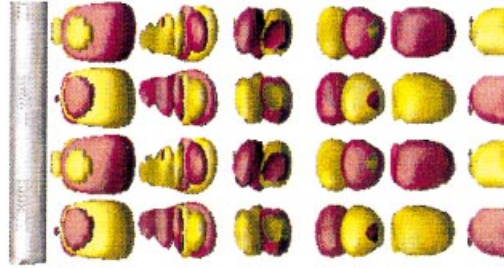
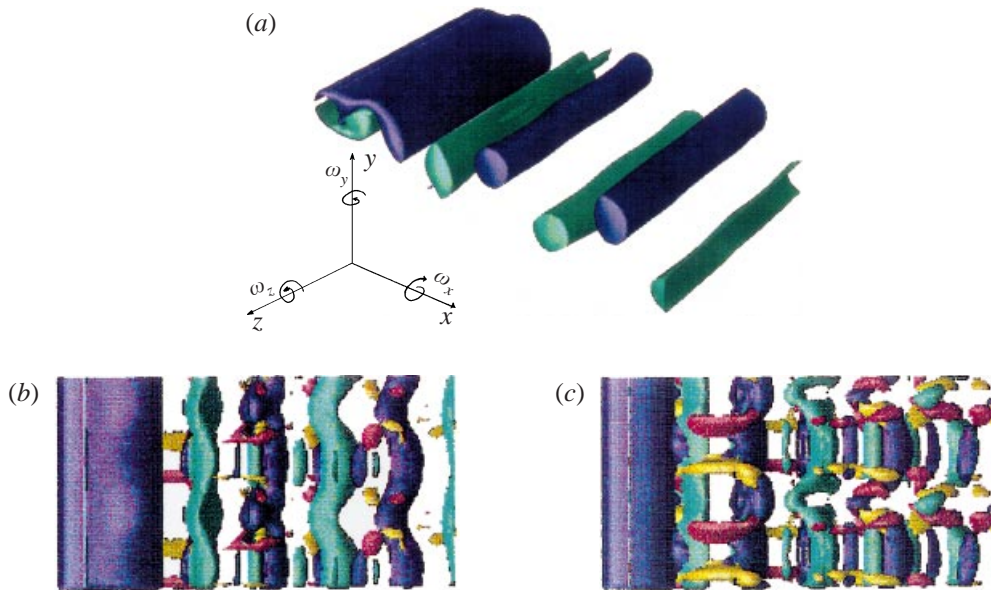FIGURE 2. Iso-vorticity surfaces, $\omega_x = 0.025$, $t = 780$.

FIGURE 3. (a) A perspective view of the vorticity field in the near wake, $\omega_x = 0.25$, $t = 780$, $Re = 220$. (b, c Iso-vorticity surfaces $\omega_x = \omega_z = 0.25$: (b) $t = 980$, compare with figure 5(b) ($s_2 = 12D$); (c) $t = 1070$, compare with figure 5(c). The spanwise length for the numerical simulations was $3.75D$; compare with figure 5(a, b, c) respectively for spanwise length $12D$.

FIGURE 4. View of the alternating and streamwise vortex structures topology in the near wake. Iso-vorticity surfaces $\omega_x = \omega_z = 0.25$.

(a)

(b)

(c)

(d)

(e)

$z = 0$

$z = 12D$

(f)

(g)
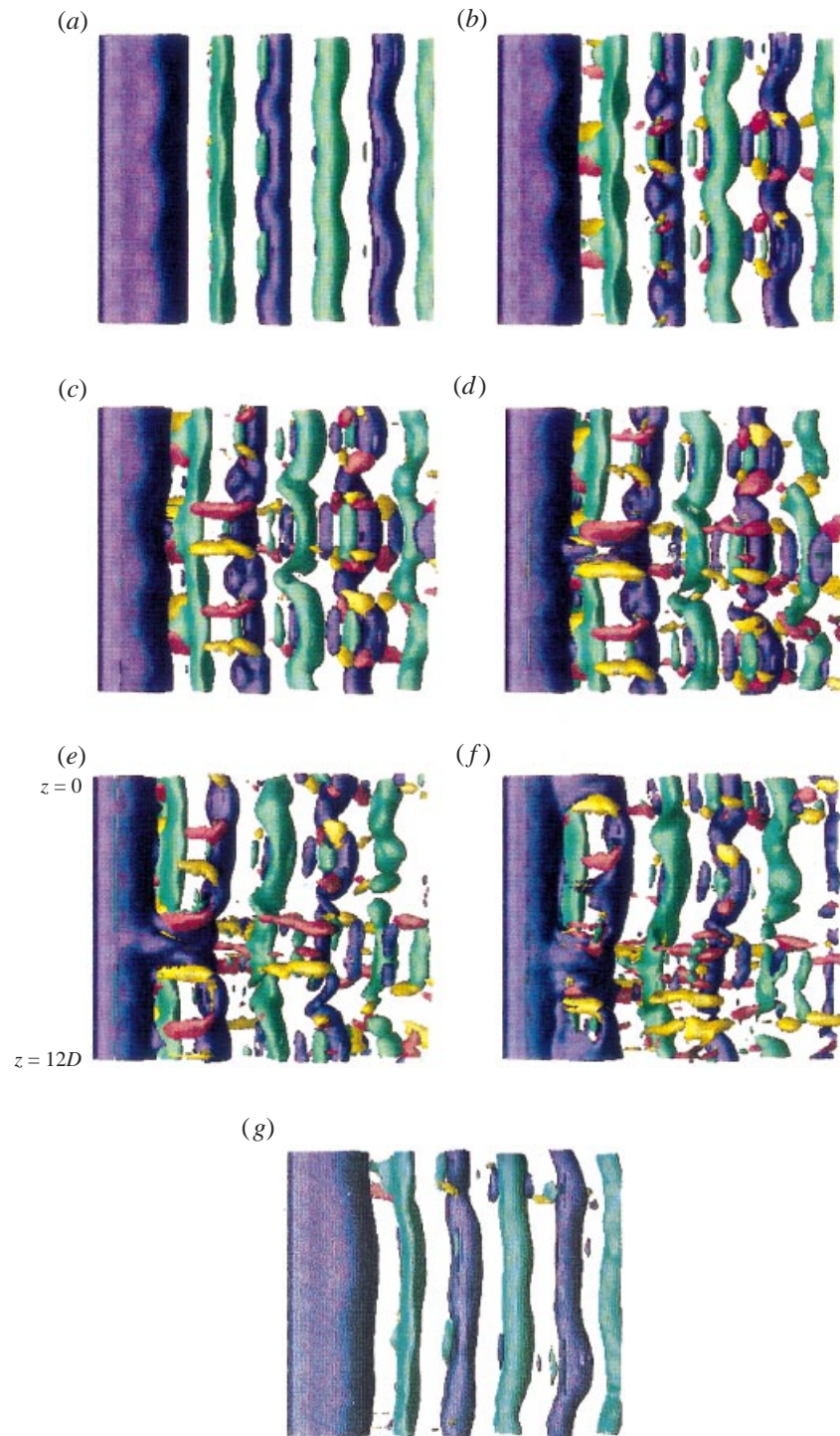
FIGURE 5. Iso-vorticity surfaces $\omega_x = \omega_z = 0.25$; (a) $t = 680$, (b) $t = 740$, (c) $t = 780$, (d) $t = 800$, (e) $t = 820$, (f) $t = 840$, (g) $t = 960$.
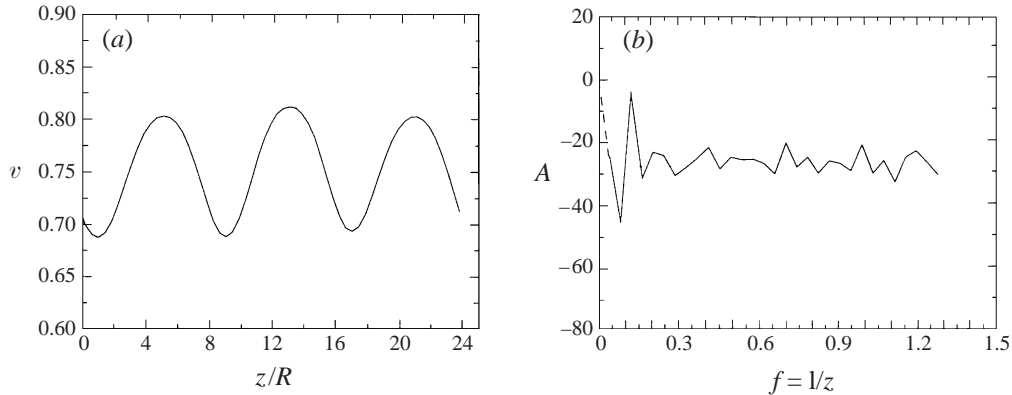
FIGURE 6. (a) Spanwise evolution of the instantaneous vertical velocity component;
(b) its spectral analysis. $x/d = 1.481$, $y/d = -0.275$.

The undulation of mode A, that occurs as an inherent characteristic of the flow obtained by the direct numerical simulation, clearly appears in the spanwise evolution of the vertical velocity component (figure 6) which displays a spanwise oscillation with a regular wavelength. In order to quantify the wavelength, a spectral analysis of this evolution is performed by means of fast Fourier transform (figure 6b). The most predominant spatial mode is found at 0.1171, corresponding to a wavelength $\lambda_z/R = 8.54$ ($\lambda_z/D = 4.27$). This value is in agreement with the range provided by experimental results, as shown in figure 8. As indicated by the experimental results, a range of mode A wavelength values exists, varying from 3 to 4.5. This dispersion is due to phases of the flow where the mode A pattern is less regular. This feature is captured by the present simulation, where mode A becomes more irregular, as for example in the time interval [800; 840]. This irregularity is associated with a further striking modification of the three-dimensional structure of the main, alternating vortex rows, analysed in §4.

The origins of the spanwise undulation have been commented on in the work by Persillon & Braza (1998b) on the basis of the Navier–Stokes fully nonlinear approach and by Barkley & Henderson (1996) on the basis of Floquet (linear) stability analysis. Their study has demonstrated that after perturbing the two-dimensional configuration of the wake vortices by Floquet modes the solution of the linearized equations of motion leads to amplification of the secondary instability and to the appearance of the spanwise undulation. The wavelength according to their study is reported in figure 8 below, together with the DNS result by Persillon *et al.* and with those from other instability theories considered in the present study. The Floquet analysis is theoretically able to take into account the mode interaction and influence of the whole topology of the vortices and it is a most promising approach. For this reason the two-dimensional configuration to be used has to preserve the *alternating vortex pattern for the whole downstream distance and not only in the very near wake and therefore to ensure the correct expansion rate of the wake*. Usually, for the sake of mesh size reduction, the alternating property is not ensured beyond one or two downstream diameters. This loses the advantages offered by the Floquet stability analysis in respect of the accuracy of the spanwise wavelength estimation.

The undulation of a single alternating vortex in the near wake can also be analysed by the elliptic stability theory as performed by Walleffe (1992) and Landman & Saffman (1987) to prove the existence of a preferred spanwise mode as a result of
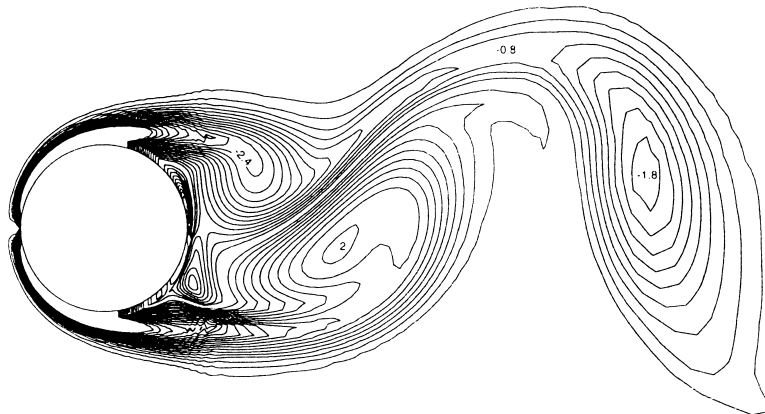
FIGURE 7. Iso-vorticity field at $Re = 220$, two-dimensional Navie-Stokes simulation (Allain *et al.* 1999), grid (266×126), showing the elliptic shape of alternating vortices and its geometric parameters for the spanwise wavelength evaluation.

spanwise-periodic small perturbations applied on an elliptic vortex configuration in the near wake. Leweke & Williamson (1998) have used Persillon & Braza's DNS data and results of the elliptic stability theory to assess qualitatively the preferred wavelength expected for the spanwise undulation. In the present study, the two-dimensional numerical results for the basic flow were produced in our research group by Allain *et al.* (1999) with a much higher grid resolution (266×126) than previous simulations. This provides an accurate order of magnitude of the maximum vorticity scale in the elliptic region and therefore an improved assessment of the spanwise wavelength. The perturbed *linearized viscous* Navier–Stokes equations are considered in the way described by Landman & Saffman (1987). It is proved that there exists a predominant spanwise wavelength mode, which is amplified from a nominally two-dimensional elliptic vortex configuration, subjected to specific geometric and dynamic constraints. It is clear that the elliptic stability theory takes into account only implicitly (through the shape of only one region of closed streamlines) the mode interaction that physically comes from the *whole alternating vortex pattern* region. Indeed, this interaction leads to a specific *elliptic* configuration of a near-wake alternating vortex (figure 7), whose geometric and dynamic parameters (vorticity and shear) enter the calculation of the secondary instability growth rate and the spanwise wavelength evaluation. The solution of the system governing the marginal stability problem gives the matrix **M** of Floquet multipliers μ_i by solving a standard ODE problem, and from μ_i the total growth rate σ_T, according to Bayly (1986). Therefore, the elliptic stability theory can be seen as a complementary way to the more complete Floquet analysis for investigating the amplification of the secondary instability. The restriction to only one elliptic vortex is of course a limitation, compared to the more general Floquet analysis, whenever the latter is applied to a physically correct alternating vortex pattern. The elliptic stability theory also takes into account the influence of the viscous decay rate in the evaluation of the total growth rate according to Landman & Saffman (1987). In the case of the secondary instability growth, there exists an ensemble of inclinations θ for the wavenumber **k** for which the wave-vector of the perturbations grows. Among these θ values, there exists an angle θ_{max} corresponding to the maximum growth rate. The parametric variation of θ_{max} versus the Eckman number $E_\gamma = 2\pi v k_0^2/g$ (k_0 being the wave-vector integration constant) has been
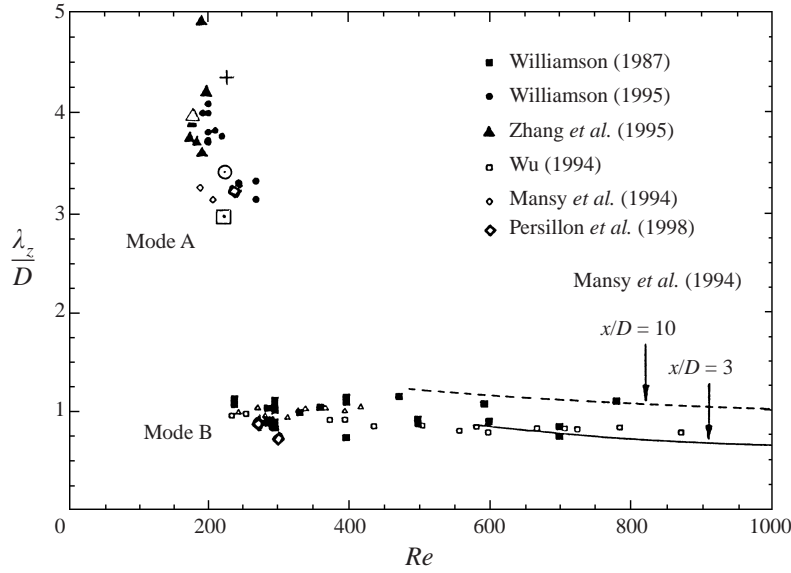
FIGURE 8. Spanwise wavelength of mode A versus Reynolds number, according to experimental studies reported by Williamson (1996) as detailed in the legend; △, Barkley & Henderson (1996), Floquet stability analysis. +, Present DNS; ⊡, present elliptic stability theory; ⊙, present Craik–Leibovich instability mechanism.

evaluated by Landman & Saffman (1987) and this variation is used in the present study in conjunction with the two-dimensional simulation data. The marginal stability curve is established through the relation $E_\gamma = E_\gamma^*(\beta)$ as a function of eccentricity. At a fixed viscosity v (corresponding in our case to Reynolds number 220) and vorticity $2\gamma = 2\omega_z$ (figure 7), β is determined for a given strain field, or equivalently by the parameter α defining the ellipsis ratio, $\beta = \varepsilon/\gamma = (\alpha^2 - 1)/(\alpha^2 + 1)$. In the case of the cylinder's elliptic vortex shape (figure 7) we find $\alpha = 0.2$ and hence $\beta = 0.6$. Therefore, the necessary and sufficient condition to have an elliptic flow, $0 < \beta < 1$, is fulfilled. The deduced length scale λ_z of the secondary instability is $\lambda_z = 2\pi/k_0 \cos\theta \approx 2l$ for moderate straining fields. The expected spanwise wavelength is $\lambda_z = 2\pi/k_0 \cos\theta_{max}$. It can also be written as $\lambda_z = l(1 + a2)\tan\theta_{max}/2 \approx 2.8$ in the present case. This result is reported in figure 8.

A complementary analysis of the origins of the present secondary instability can be found by analogy with the Craik–Leibovich instability mechanism (Craik 1982a, b). The principles of this mechanism are based on the Stokes drift s_d and the effect of spanwise-periodic small perturbations. Stokes drift occurs through the shearing mechanism upstream of an undulated periodic flow (flow over waves or hills), $s_d = (u^L - u^E)$, where u^L is the Lagrangian mean velocity and u^E the Eulerian one. The presence of the wavy (x, y) pattern is decisive in the development of the Craik–Leibovich instability, because it causes the difference between the Lagrangian-mean and Eulerian-mean flows, which creates the longitudinal vorticity (Craik 1982b). The Stokes drift is taken into account by means of the generalized Lagrangian mean (GLM) equations of motion as shown by Andrews & McIntyre (1978a, b). The perturbation of the two-dimensional periodic wavy flow by spanwise-periodic small perturbations of type $u' = \Delta\mathrm{Re}(e^{\sigma t}e^{i\lambda_z}[\hat{u}(y), \hat{v}(y), \hat{w}(y)])$ leads to solving the Rayleigh equations to detect the most unstable spanwise wavenumber. The streamwise vorticity
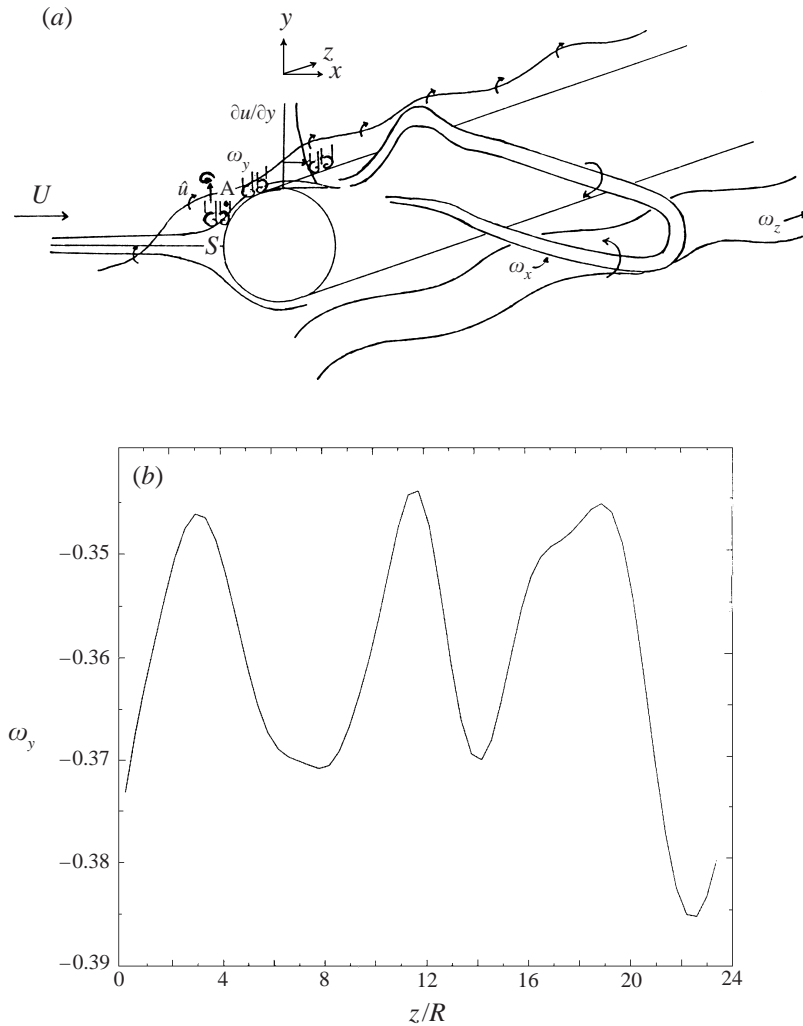
FIGURE 9. (*a*) Sketch of the production of streamwise vorticity filaments ω_x, by stretching and tilting through the main shearing mechanism u/y (due to the bluff body form), acting on the vertical vorticity ω_y. The vertical vorticity was previously created in the vicinity of the stagnation region upstream, under the action of the spanwise small perturbations. (*b*) Spanwise evolution of the vertical vorticity component ω_y at point A ($t = 800$) according to the sketch on figure 10.

is therefore subjected to exponential growth, created by the action of the mean shear that produces rotation and stretching of the vertical vorticity.

This mechanism is physically realizable, and was originally studied in the experimental and theoretical work of Jackson (1973). He showed that a flow over a two-dimensional block systematically develops streamwise counter-rotating vortices like the trailing vortices of a horseshoe configuration. More recent experiments by Gong, Taylor & Dörnbrack (1996) also showed that the mechanism creating the streamwise vortex pairs is related to the amplification of the spanwise-periodic small perturbation of u velocity, of the type $\hat{u} \propto e^{ikz}$ in the vicinity of the stagnation region, *leading to the development of longitudinal vorticity through stretching and tilting of the vertical vorticity*, as analysed in the work of Sadeh & Brauer (1980) and according
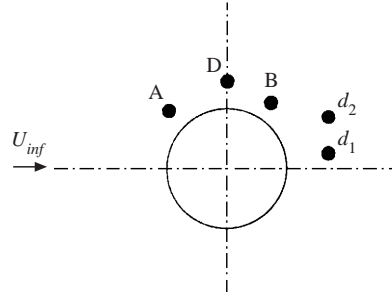
FIGURE 10. Sketch of selected positions upstream and downstream of separation, to study the spanwise evolutions of the different flow quantities.
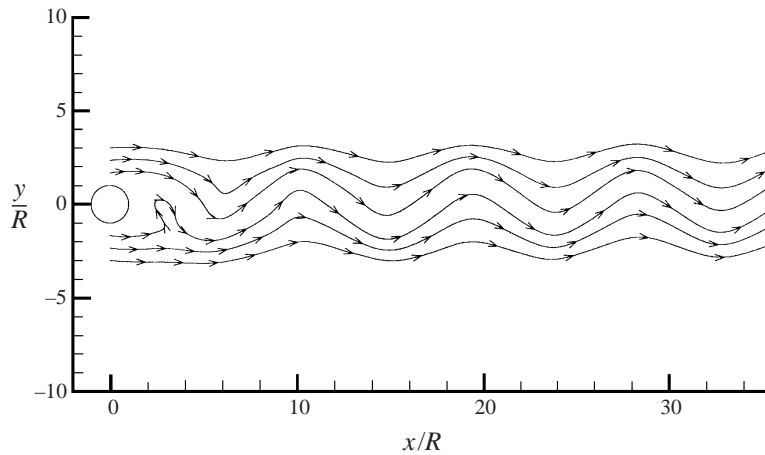

FIGURE 11. Instantaneous streamline pattern in the near wake, illustrating the formation of a 'wavy terrain', $Re = 220$.

to discussions with J. C. R. Hunt (1999, personal communication). In the case of the cylinder wake, this is schematically presented in the diagram of figure 9(*a*). The present DNS indeed shows an amplification of the vertical vorticity in the vicinity of the stagnation region, according to the quasi-periodic pattern along the span (figure 9*b* and 10). The analogy with the cylinder wake can be further based on the existence of the strong shearing mechanism generated upstream the wake by the obstacle, as well as by the related Stokes drift. The wavy terrain downstream is formed by the undulated streamline pattern (figure 11) due to the alternating vortices, over the whole downstream distance.

This provides an evaluation of the streamwise wavelength λ_x due to the periodicity of the von Kármán vortex pattern. This parameter, in conjunction with the free shear layer thickness δ, enters the calculation of the most unstable spanwise wavenumber, according to the results by Phillips, Wu & Lumley (1996). It is then possible to derive that there exists a locus of a (minimum l – minimum α) combination at which a significant growth rate σ_1 occurs; l is the spanwise dimensionless wavenumber, $l = 2\pi\delta/\lambda_z$, and α the dimensionless streamwise wavenumber, $\alpha = 2\pi\delta/\lambda_x$. This locus is given by Phillips *et al.* (1996) in their figure 5 for a 1/7-power law velocity profile, and can be used to derive the expected spanwise wavenumber of the secondary instability, as a function of the longitudinal wavenumber α. In the case of the cylinder
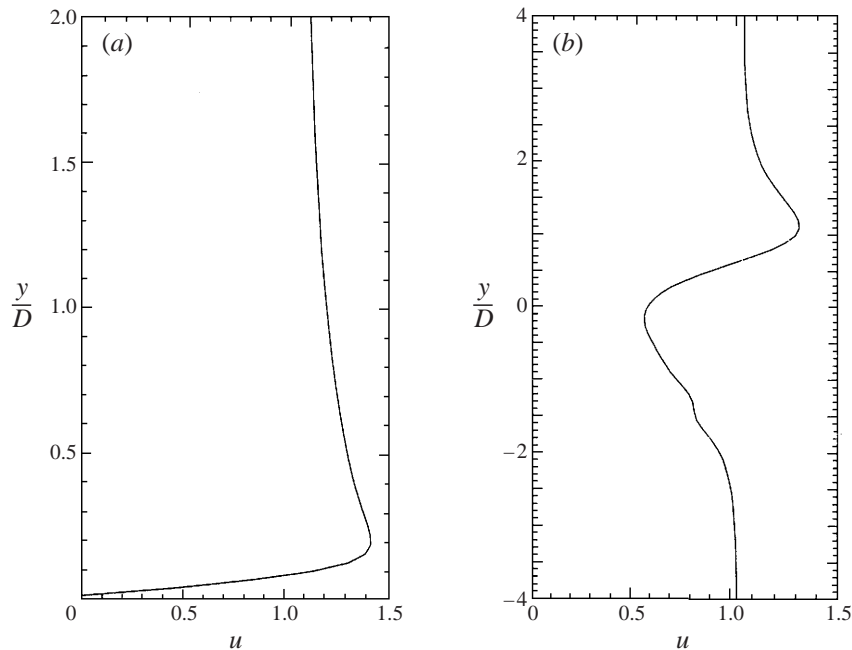
FIGURE 12. Instantaneous longitudinal velocity profile at (*a*) $x/D = 0$ and *b*) $x/D = 5$; $Re = 220$, two-dimensional case.

wake, to estimate the effective shear layer thickness δ related to this waviness, the u velocity is plotted in at $x = 5D$ (figure 12), corresponding to a crest of the wavy configuration, as in the study by Phillips *et al.* (1996). The shear layer thickness is measured from the $y/D = 0.5$ axis corresponding to the main shearing source due to the cylinder shape. δ/D is found to be of order 0.6 and α of the order of 0.8, given that $\lambda_x = 4.7D$ from the two-dimensional basic flow simulation. The resulting spanwise dimensionless wavenumber l is found to be 1.1. This yields $\lambda_z = 3.4D$ for the cylinder wake.

The feedback effect between the sustenance of the streamwise and vertical vorticity is strongly taken into account by this instability mechanism and clearly shown by the present direct simulation (Allain *et al.* 1999) where the amplification of upstream vertical vorticity and downstream streamwise vorticity are shown as a strongly maintained spanwise-periodic mode. The Craik–Leibovich instability mechanism analyses the birth of the streamwise-periodic vorticity by taking into account *the nonlinear effects through the inviscid mechanism* described by the Rayleigh equations. The nonlinearity is not taken into account by the Floquet analysis or by the elliptic stability theory. These effects are however strongly involved in the irreversible nature of the three-dimensional bifurcations undergone by the present system. Therefore, this instability analysis can be seen as a complement to the previously mentioned theories. Although it is applicable in the regions of open streamlines (e.g. beyond the very near wake), it involves the global interaction of modes coming from the *alternating* pattern over a significant downstream distance in the wake.

The three types of instability processes mentioned above need the use of results from the two-dimensional full Navier–Stokes simulation concerning the basic flow and all these approaches perturb the alternating vortex configuration by spanwise-periodic small perturbations. The wavelengths assessed by these theories provide results close
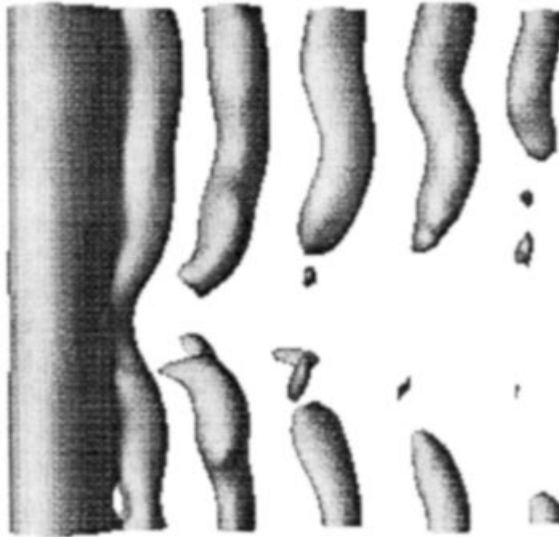
FIGURE 13. Iso-pressure coefficient surfaces, $C_p = -0.25$, $t = 820$.

to those from a complete direct numerical simulation approach (figure 8). All the instability theories mentioned lead to a complementary comprehension of the physical mechanisms involved in the creation of the spanwise undulation of nominally two-dimensional alternating vortex rows.

4. The natural vortex dislocations pattern

In this section, a substantial modification of the main spanwise undulation is analysed as a systematic phenomenon of the three-dimensional transition. The instantaneous iso-vorticity fields ω_z and ω_x are considered first. (The orientation of vorticity components is shown in the sketch of figure 3.) During the time interval [800; 820], figure 5(d, e), a remarkable phenomenon is seen, concerning the braid configuration of the red and yellow spanwise vortices, which progressively ejects fluid from the first violet main eddy. Simultaneously, this braid structure is displaced to a lower position. Under this action, a clear discontinuity is obtained along the core of the second main violet vortex, and this discontinuity persists until the time value 840 (figure 5f). The braid of streamwise vortices loses its spatial coherence during the time interval [820; 840] (figure 5e, f) and simultaneously, the overall streamwise vortex structures are much more fragmented even in near-wake positions. During these phases of the flow, mode A is no longer regular. The break in the continuity of the vortex core can also be seen in figure 13 where the iso-surfaces of the pressure coefficient are presented. This local spanwise discontinuity is related to an adverse pressure bump locally formed along the span, to be discussed in detail in §4.2. These effects are directly associated with the observed discontinuity in the main vortex filaments. This fundamental modification occurring on the spanwise structure of the main vortex rows in the near wake is called a *natural vortex dislocation*, due to a very close similarity with the experimentally obtained flow visualizations of this kind of structure by Williamson (1992), figure 14. In his study, the existence of 'spot-like' natural vortex dislocations was indicated, but their systematic development during
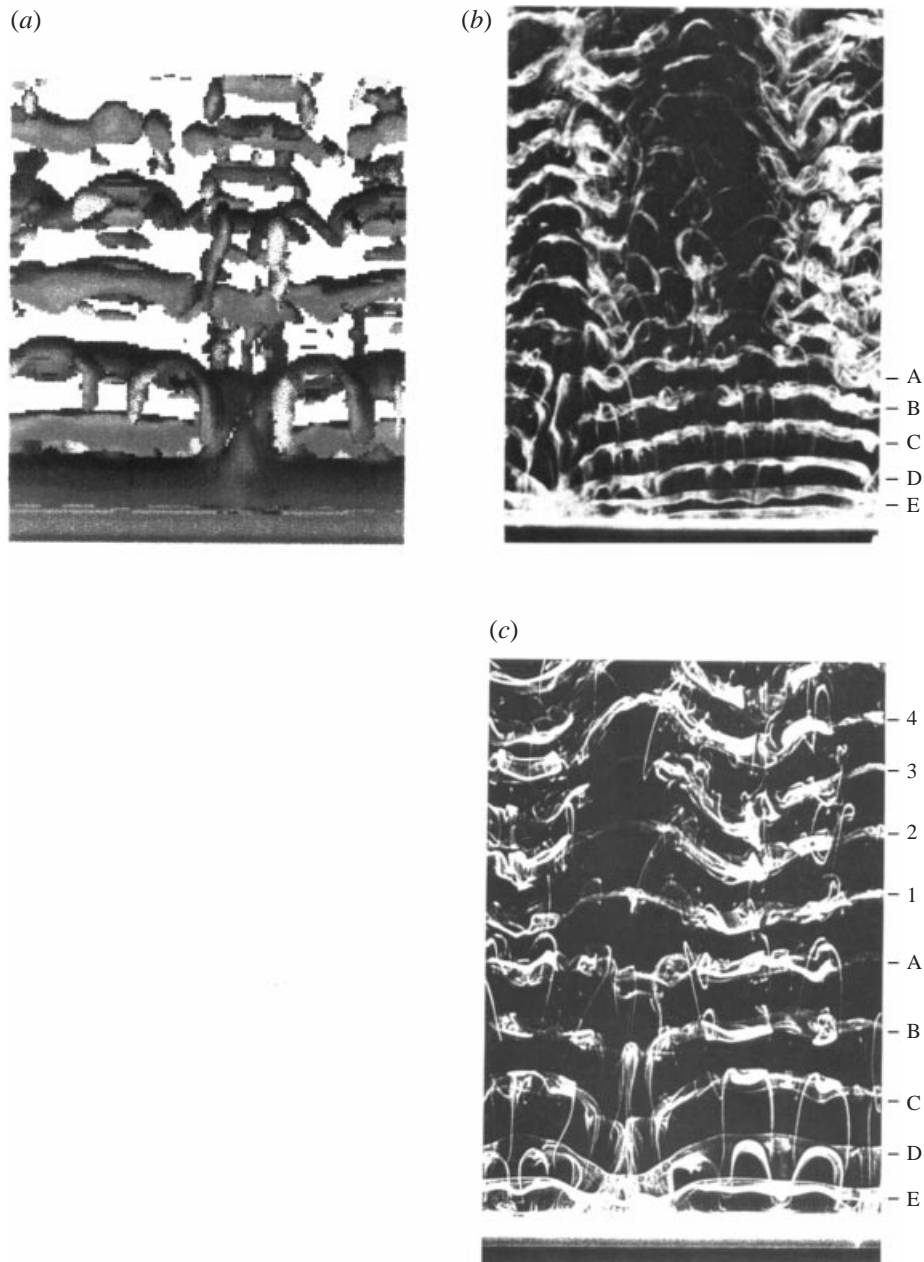
FIGURE 14. Views of a natural vortex dislocation pattern: (*a*) results obtained by the present direct numerical simulation; (*b*) experimental visualizations, Williamson (1992); (*c*) figure provided by courtesy of C. Williamson, 1998, private communication: formation of vortex dislocation (rows D, E) and a more chaotic state concerning the longitudinal small structures and mode A undulation (rows C, B, A) follows by the return to more regular, quasi-periodic mode A undulation (rows 1, 2, 3, 4).

the three-dimensional transition has not been shown up to now. In Williamson's study only *forced dislocations* were analysed, in order to strengthen their dynamic characteristics and their visibility. In the present study the vortex dislocations are obtained *naturally* by means of the complete Navier–Stokes simulation. This is an originality of the present study since, to our knowledge, natural vortex dislocations have not been obtained yet by other three-dimensional simulations. Henderson (1997) argues that these structures do not exist in the near wake in the present Reynolds number range despite the experimental evidence. He depicts phase irregularities of vortex rows especially at a higher Reynolds number ($Re = 1000$), which have no similarity with the experiments.

As can be seen in figure 15 ($t = 804$ and 808), the occurrence of natural vortex dislocations is regular in time and alternate positive (violet) and negative (green) vortex dislocations are formed. Moreover, large-scale spanwise cells are formed due to the appearance of more than one location of vortex dislocations along the span (figure 5*f*). Of course, an even higher spanwise length would be needed in order to determine the typical length of this kind of large cell, but this task would demand a CPU time beyond the possibilities of the present study.

Summarizing the main features that qualify this modification as a vortex dislocation, it can be stated that this kind of structure is a local break of continuity appearing on 'the spinal column' of a main vortex row, previously subjected to a regular spanwise undulation. This three-dimensional modification appears as a local junction with the previous alternating vortex row, inducing *locally a 'number of events* −1' in the vortex shedding process and therefore a substantial fundamental frequency reduction, quantified in §4.1. It is found that mode A loses its spatial coherence at phases of the flow following the formation of a vortex dislocation (figure 5*f*). The present simulation illustrates variations in mode A waviness. At phases of the flow following the development of vortex dislocations it can be seen that the braid structure of streamwise vorticity almost disappears to give way to more fragmented streamwise structures of even smaller vortices. In these intervals it can be seen that the waviness of the main vortices becomes even more fragmented along the span, but after the passage of the dislocation it is found that the vortex rows start to form the main spanwise undulation again, as can be seen at larger times, figure 5(g), $t = 960$. Moreover, as is shown in the time-dependent evolution of the velocity components (figure 16, 20 top), the flow again attains its quasi-periodic character after the passage of the dislocations. The positions 1 to 3 marked in figure 16 indicate the spanwise region where vortex dislocations are developed. It is shown that w component at these positions presents a considerable amplitude increase and loses its periodic character during the time intervals corresponding to the formation of vortex dislocations, to recover the quasi-periodic character at longer times. Amplitude and frequency modulations are also obtained on the v velocity signals in the same time intervals. Therefore, it is found that the dislocation phenomenon is indeed associated with large-scale velocity fluctuation irregularities interspersed among quasi-periodic regions, a feature that had been observed by Roshko (1954) in the same category of flows and linked to the onset of three-dimensional effects. From this overall flow evolution, it can be seen that, due to the vortex dislocations, the occurrence of mode A has an intermittent character, which also explains the dispersion of experimental wavelength values (figure 8). Therefore, the flow evolution reaches cyclically a quasi-periodic stage, alternating with a more chaotic one in respect to the vortex dislocations formation. This feature is in good qualitative agreement with flow visualizations by Williamson (1992, figure 14*c*), where smaller scales become more fragmented in the
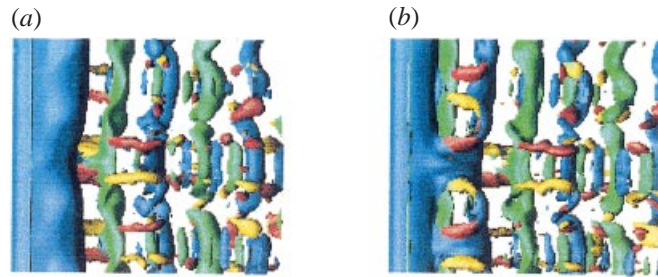
(a) (b)

FIGURE 15. Iso-vorticity surfaces $\omega_x = \omega_z = 0.25$ at (a) $t = 804$ and (b) $t = 808$, tracking the successive formation of vortex dislocations on opposite-sign main vortices.

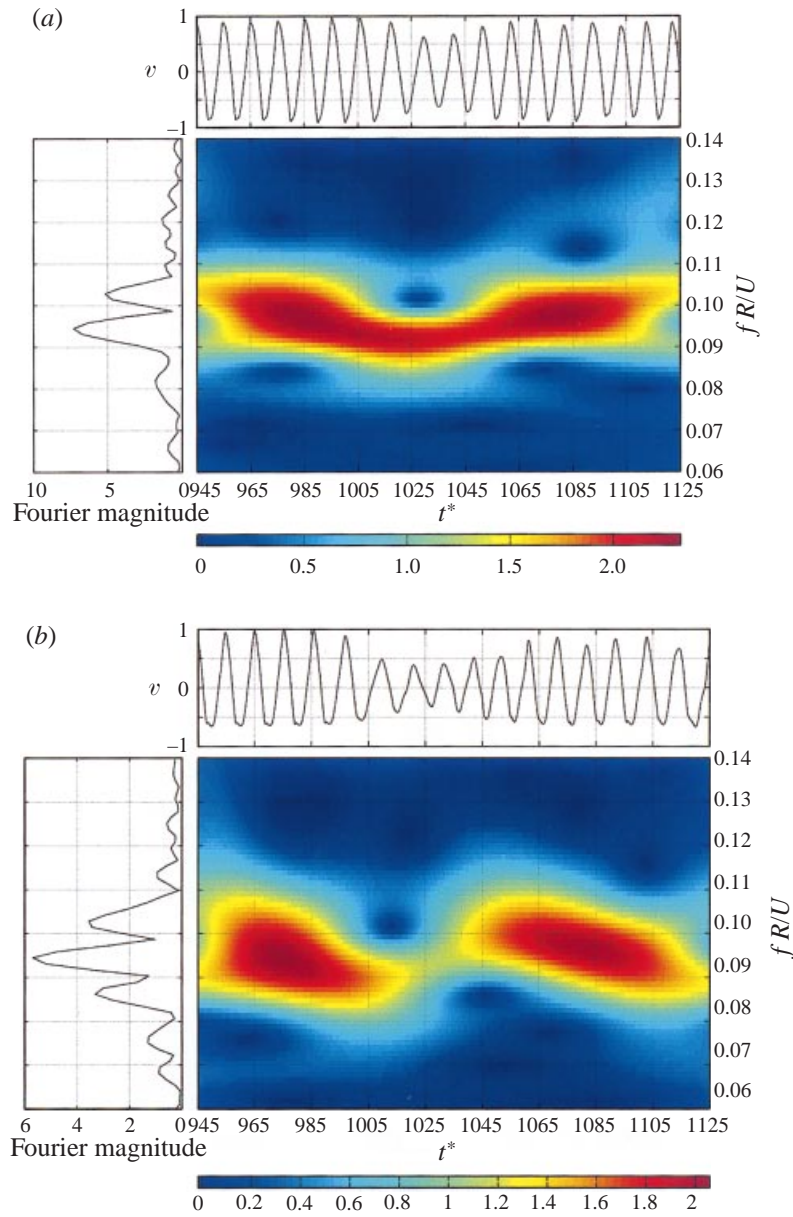
FIGURE 22. Wavelet analysis of the v velocity signal: (a) at $(x/D, y/D, z/D) = (1.5, 0.303, 0.1)$; and (b) at $(x/D, y/D, z/D) = (1.5, 0.303, 7.5)$.
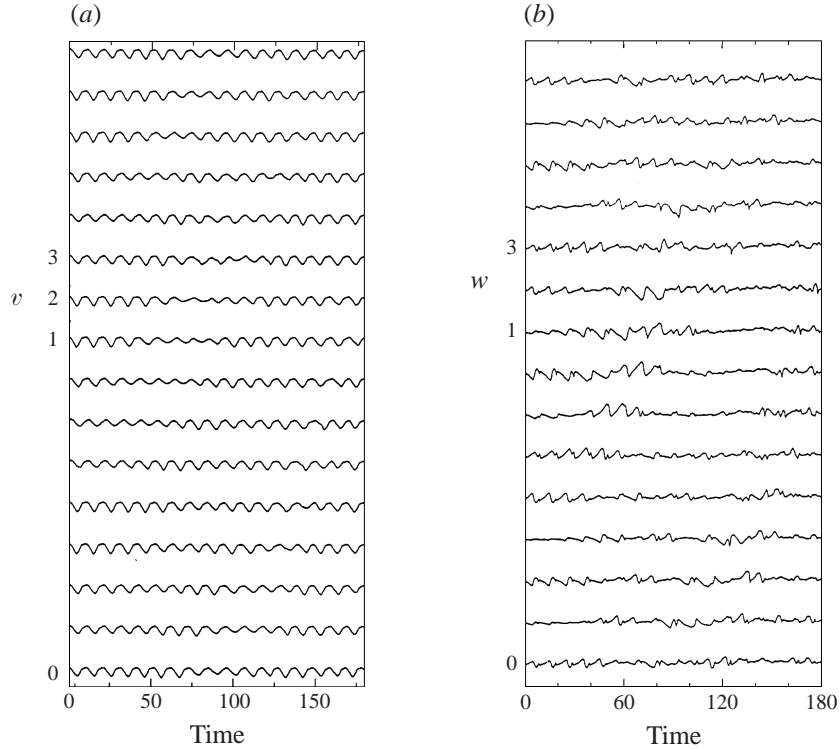
FIGURE 16. (*a*) v component versus time at 16 equidistant z positions along the span, $(x/D, y/D) = (1.52, -0.5)$. (*b*) w component. Spanwise positions 1, 2, 3 mark the region of formation of dislocations. Amplitude and frequency modulation occurs within time interval 50–100 corresponding to the passage of a dislocation. The time-origin $t = 0$ corresponds to the dimensionless time value 770.

downstream vicinity of the dislocation formed on rows E and D (see longitudinal vortices on C, B, A main vortex rows) and the spanwise undulation is less regular on these vortex rows than much farther downstream (rows 1, 2, 3, 4) where regularity is progressively reached again. An absolutely regular appearance of the spanwise mode would be in fact an artificial organized feature which scarcely happens naturally.

4.1. *Time–frequency analysis*

In this section, the modification of the orderly structure of the velocity and vorticity signals is quantified as a function of time and of spanwise location, with a view to tracking the development of vortex dislocations and their influence on mode A. This task is carried out first by producing a spectral analysis of the temporal evolution of the velocity and vorticity along the span; secondly, by means of wavelet analysis and of autoregressive modelling techniques, in order to quantify the variations of frequency and amplitude as a function of time; thirdly, by discussing the properties of the different flow quantities on (z, t) maps.

4.1.1. *Spectral analysis*

In order to examine the global behaviour of the fundamental mode along the spanwise direction, a fast Fourier transform was performed on the v component signals at (x, y) coordinates equal to $(x/D = 1.5, y/D = 0.303)$. 900 points were used, corresponding approximately to 100 times the vortex shedding period. The
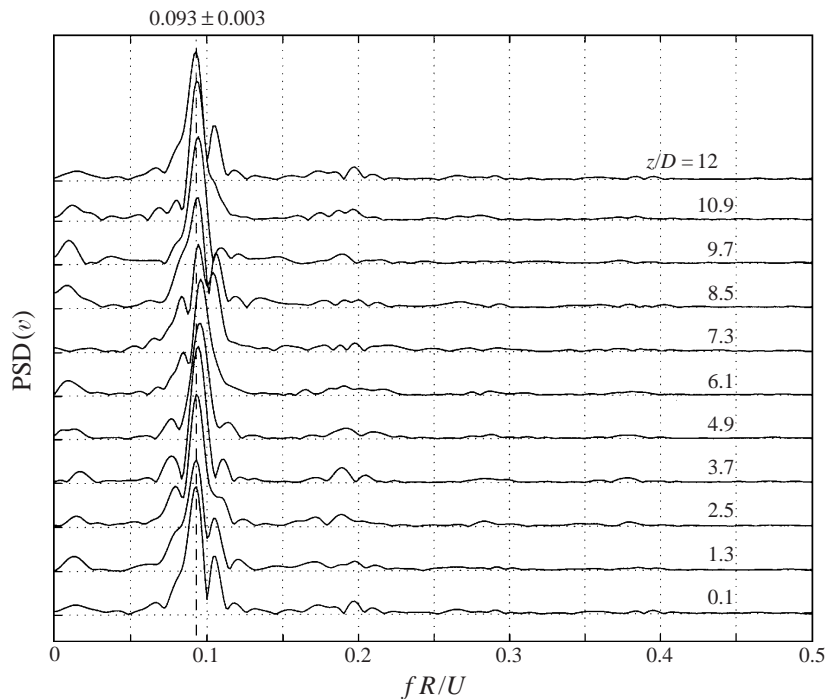
FIGURE 17. Spectra of the v component along the span at point $(x/D, y/D) = (1.5, 0.303)$.

dimensionless length of time series was 0.2 and the dimensionless frequency accuracy was 0.005. Note that a considerable CPU time has been dedicated (typically about 100 hours on an IBM-SP2 computer) to the present analysis. In figure 17 the spectra are shown along the spanwise direction. The fundamental frequency appears as the predominant one at all z positions examined. It is found that the spectral energy of the fundamental is not constant along the span and that it reduces considerably in the regions where a vortex dislocation occurs (see figures 17 and 18 at z/D in the vicinity of 2 and $4 < z/D < 10$).

The spectra of the ω_z vorticity component are analysed in figure 19. The same behaviour as for the v component is obtained concerning the spectral energy distribution along the span. In these spectra, apart from the fundamental, the first harmonic also appears as a less dominant yet distinguishable frequency. This is due to the influence of the u component, present in the expression for ω_z. This component is affected simultaneously by the passage of both lower and upper alternating vortex rows at the present (x, y) position. It is also found that less energetic distinguishable frequency peaks appear in the vicinity of the fundamental, at lower and higher frequency values, and that these peak amplitudes become more pronounced for spanwise positions associated with the decrease of the fundamental's spectral energy. As will be discussed below, this energy reduction of the fundamental and the associated peaks is related to the appearance of the vortex dislocations, an event which perturbs mode A undulation and 'pumps' a fraction of the fundamental's energy. This process will be tracked by means of a time–frequency analysis of the signals issued by the direct simulation.
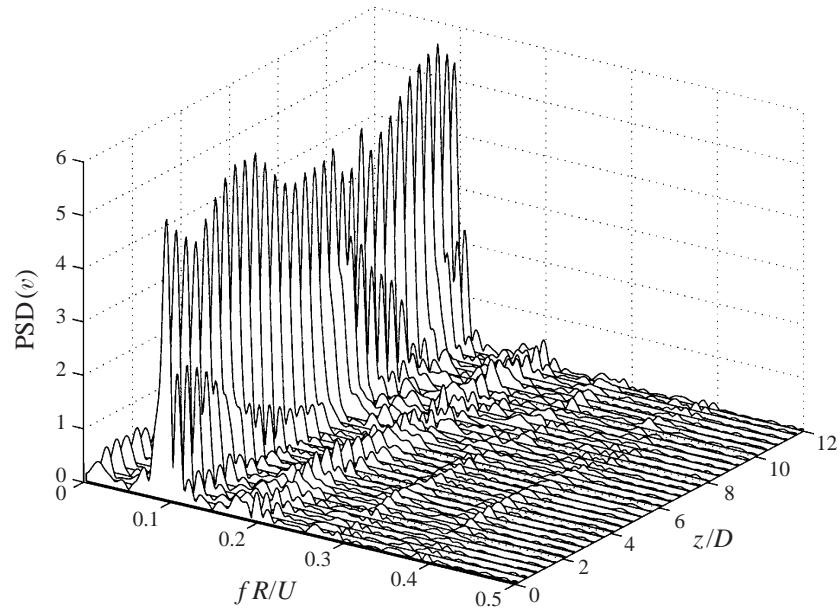
FIGURE 18. A perspective view of the spectral energy variations in the spanwise direction.
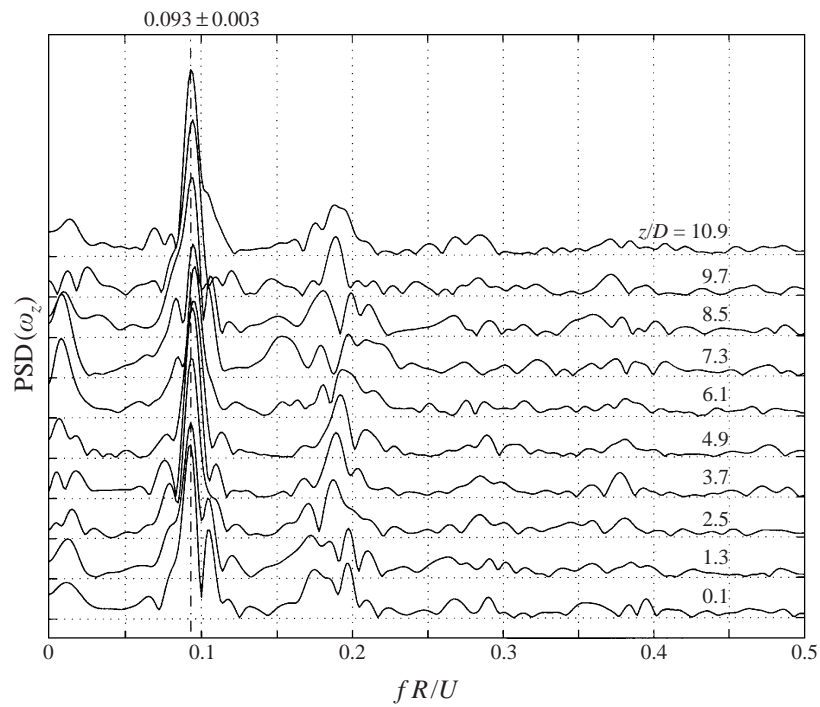

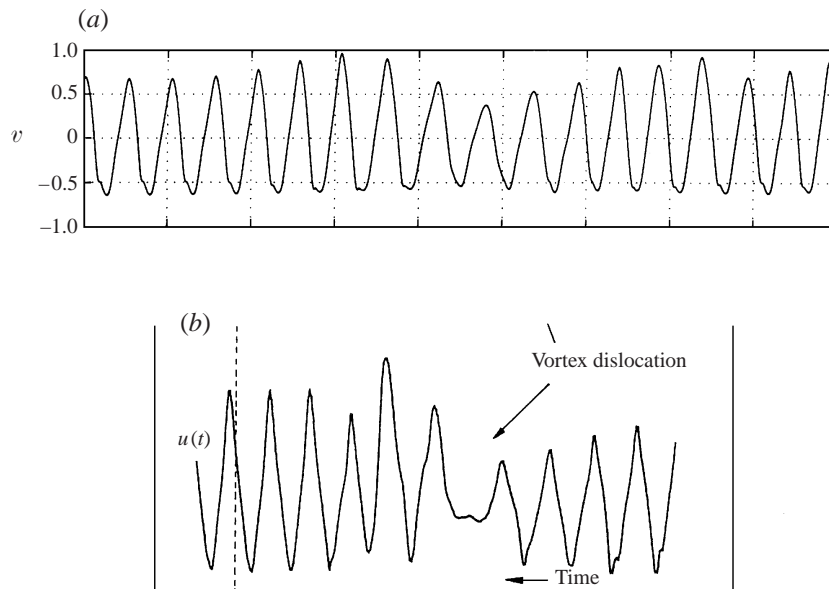FIGURE 19. ω_z vorticity component spectra in the spanwise direction at point $(x/D, y/D) = (1.5, 0.303)$.

FIGURE 20. Velocity signals showing modulations due to the passage of a vortex dislocation: (*a*) results of the present direct simulation; (*b*) experimentally obtained velocity signal, Williamson (1992).

4.1.2. *Quantification of the fundamental frequency versus time*

A typical signal of the v velocity component is presented in figure 20. The analysis point at $(x/D = 1.5, y/D = 0.303)$ is chosen in the (x, y) plane for all z positions examined. In the following figures, the dimensionless frequency is normalized with respect to the cylinder radius. The vertical velocity component is chosen for the analysis, because it responds immediately to the passage of a von Kármán vortex row and it is not 'masked' by the upstream convection velocity as in the case of the u component. It is clearly seen that the structure of the signal is modified in the dimensionless time interval [1000; 1050]. It is noticeable that a qualitatively similar modulation occurs in the experimentally obtained time-domain signal (figure 20) reported by Williamson (1992).

In the following, as well as a standard spectral analysis which gives the global frequency behaviour of the time-dependent evolution of the different flow quantities, it is essential to quantify the variations of frequency and amplitude versus time. This is done by performing autoregressive modelling signal processing and wavelet analysis on the signals obtained by the present direct simulation. In this part of the study, due to an initial time value which had been inserted in the processing, the reader should note that the time history from 945 to 1125 is equivalent to the time interval [760; 1040], shifted by 185. In this way, a direct correspondence of the time values of figures 1 to 5 (the contour plots of the flow quantities) and of the figures of this section is obtained.

Figure 21 presents the frequency variation versus time of the v component, by using an autoregressive model (AR), according to which the signal is modelled by the response to a white noise passed through the autoregressive model. After different tests, a fourth-order model has proved sufficient to describe the signal (see the Appendix). This method is applied at successive time intervals (windows) of the signal, the windows having a mean individual length of 20. This kind of model
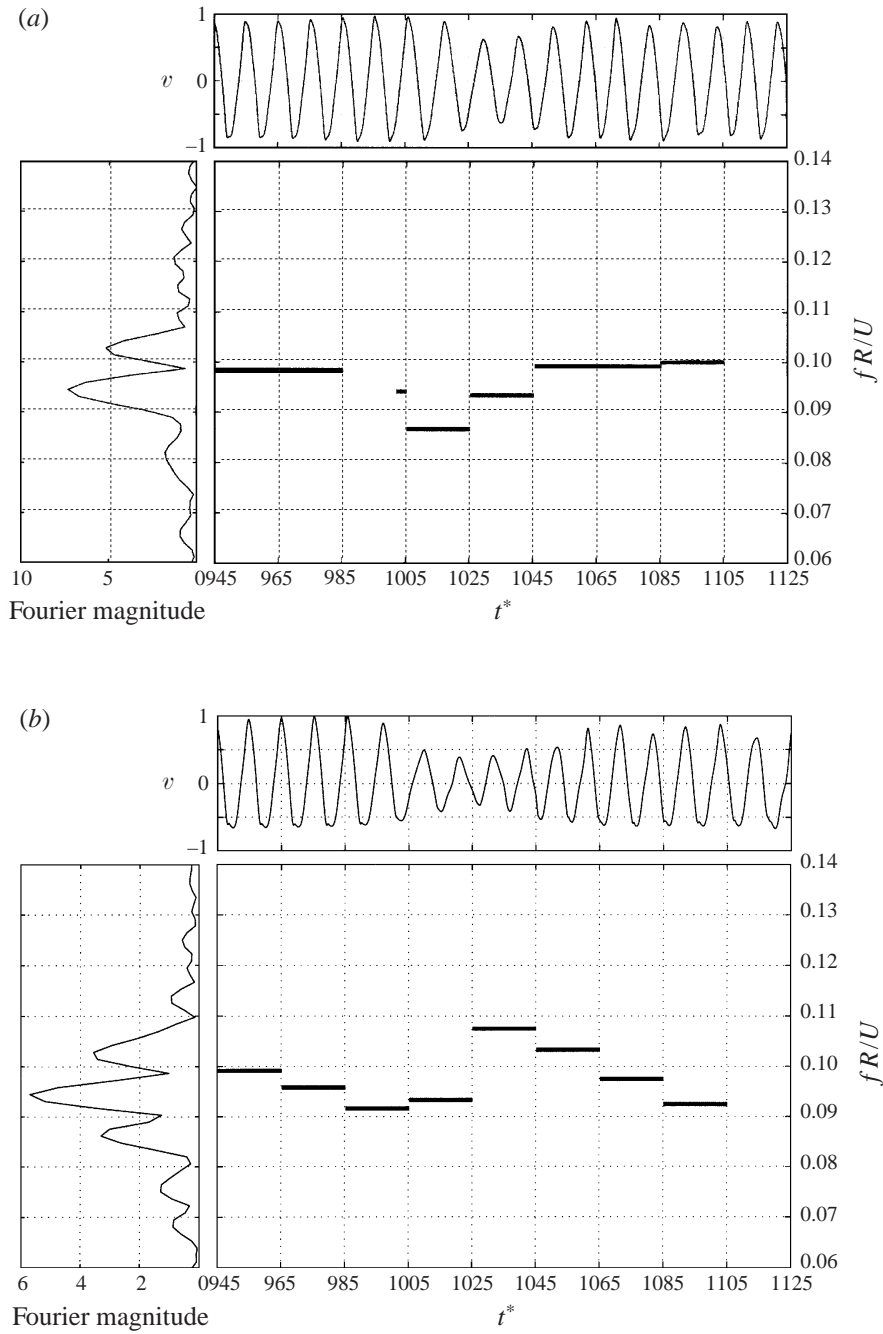
FIGURE 21. Time–frequency analysis of the v component signal by using autoregressive modelling (AR): (a) $(x/D, y/D, z/D) = (1.5, 0.303, 0.1)$; ($b$) $(x/D, y/D, z/D) = (1.5, 0.303, 7.5)$.

conceptually ensures a high accuracy in the estimation of the frequency values versus time, even for a moderate number of time-domain samples. In the present case, it provides 10^{-4} time accuracy, as mentioned in the Appendix. In figure 21 it is clear that the fundamental frequency undergoes a considerable and abrupt reduction within

the time interval $[1000; 1050]$, corresponding to the passage of the vortex dislocation (figures 5*d* and 5*e*). This feature is confirmed by applying a Morlet wavelet analysis to the same signal (see Grossman, Morlet & Paul (1985) and the Appendix of the present article). In addition to the frequency reduction obtained (figure 22), the wavelet analysis provides the distribution of the energy density on the time–frequency map. Therefore, the wavelet analysis is expected to give the amplitude modulations in more detail, whereas the autoregressive model analysis provides a better description of the variations of frequency versus time. Hence the two techniques are complementary in examining the signal modulations occurring during the passage of the vortex dislocations. In figure 22 (see p. 19) the kernels of high density (dark red) correspond to the parts of the signal before and after the dislocation occurrence, where the fundamental mode is the most energetic and related to the highest amplitude values. These parts of the signal correspond to the organized, coherent motion. The more central area of the map is characterized by a density decrease, associated with the amplitude decrease on the passage of the dislocation. It is also found that the area of maximum density (dark red) moves towards lower frequency values within the central area of the plot. This also illustrates the frequency reduction occurring in the interval $[1000; 1050]$, as obtained by means of AR modelling. This behaviour indicates that the frequency decrease event, occurring upon the passage of the vortex dislocation, is also characterized by a relatively strong degree of coherence and is therefore associated with this kind of vortex structure.

The spectrum of the signal is also shown on these figures. The most predominant frequency is the fundamental vortex shedding Strouhal one. In addition, a second dominant peak corresponds to a slightly accelerated shedding phase which follows the passage of the dislocation. This happens in order for the whole system, which behaves as a global oscillator, to be able to compensate the delay caused to the shedding mechanism by the vortex dislocation. This acceleration effect on the vortex shedding is better shown by the AR model in figure 21(*a*). Moreover, the smaller frequency peak on the left of the fundamental corresponds to the global effect of the frequency decrease analysed above. In figure 21(*b*) ($z = 7.5D$) a second event of frequency reduction appears towards the end of the time history.

By examining the spectrum at this position and also at a number of points along the span, it can be seen that the spectral energy has been split into three peaks at spanwise positions corresponding to formation of a vortex dislocation and so the energy level of the fundamental has been reduced. This can be seen more clearly in figure 21(*b*), where the three peaks are pronounced and correspond typically to a beating phenomenon where the middle frequency corresponds to the mean frequency $0.5 \times (f_1 + f_2)$, f_1 and f_2 being the lower and the higher frequencies respectively. This splitting and the associated amplitude modulation occur during the passage of the vortex dislocation. f_1 is due to the frequency delay as quantified by the autoregressive analysis and by wavelets, because of the formation of the vortex dislocation. f_2 is due to the acceleration of the vortex shedding along the vortex rows below and above the vortex dislocation in order to 'catch up' with the frequency delay and to realign the value of the nominal Strouhal number in the areas without dislocations. These sidebands in the frequency peaks are related to Floquet modes that would amplify along the span as shown by a Floquet analysis of the basic two-dimensional alternating flow at $Re = 220$ from the present Navier–Stokes simulation. The system would be subjected to an upstream longitudinal non-uniform u velocity boundary condition along the span, obeying a specific distribution of the u component as discussed at the end of §4, to produce the effect of the vortex dislocations. Also recall that from
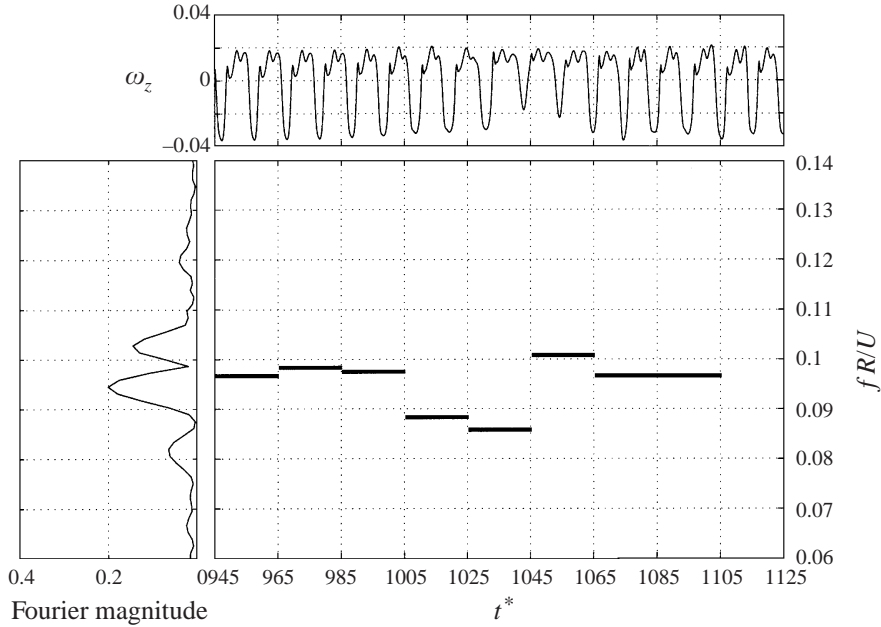
FIGURE 23. AR analysis of the ω_z time-history at $z/D = 0.7$.

standard signal processing considerations, the splitting of the spectral energy into the three peaks corresponds to a significant amplitude modulation in the time domain, and this in fact happens in the interval $[1000; 1050]$ as can be seen in figure 21(b), where a second vortex dislocation occurrence is detected towards the end of the time history. Therefore, the splitting of the spectral energy into three peaks (and the associated amplitude modulation) occurs during the passage of the vortex dislocation and a result of this distribution is, as expected, a reduction of the spectral energy available to the fundamental. This behaviour characterizing the dislocation regions can be seen in the spanwise representation of the spectral energy (figure 18). At all the positions examined by means of autoregressive modelling analysis, each frequency reduction is followed by an acceleration (frequency increase) of the fundamental mode. This allows the overall vortex shedding process to 'readjust' its delay in order to obey the global shedding frequency law corresponding to the present Reynolds number. The frequency reduction and the amplitude modulation are illustrated by both autoregressive modelling and wavelet analysis, the AR modelling showing more intensely the frequency reduction and the wavelet analysis showing more clearly the amplitude decrease, during the passage of a vortex dislocation.

Time series of the ω_z vorticity are also examined by a time–frequency analysis in figures 23 and 24(a, b). The vorticity signals are indeed a very good 'tracer' to illustrate the time variations occurring within the spinal column of each main vortex row, which may be considered as a solid solenoidal body, where the Biot-Savart law qualitatively applies. It is found that the passage of a vortex dislocation is also associated in this case with a noticeable frequency reduction of the fundamental mode, and of a considerable amplitude modulation, quantified in the present vorticity component signals. Figure 24(b) shows the same beat phenomenon, where the amplitude modulation corresponds to a two-lobe wavelet configuration as for the v signal in figure 22. The frequency reduction effect is shown in this configuration by the fact
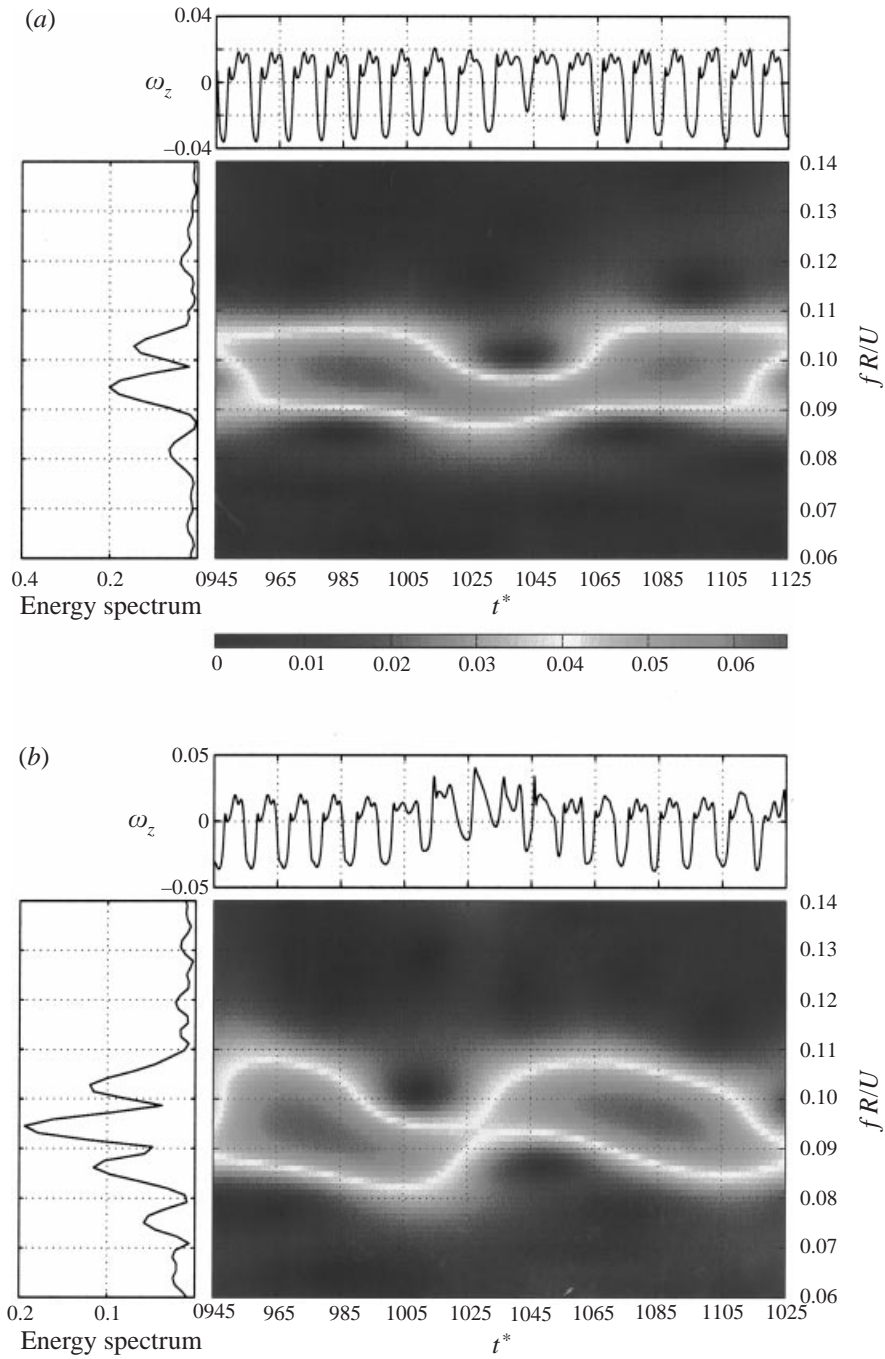
FIGURE 24. Wavelet analysis of ω_z vorticity signal: (*a*) at $(x/D, y/D, z/D) = (1.5, 0.303, 0.7)$, and (*b*) at $(1.5, 0.303, 7.5)$.
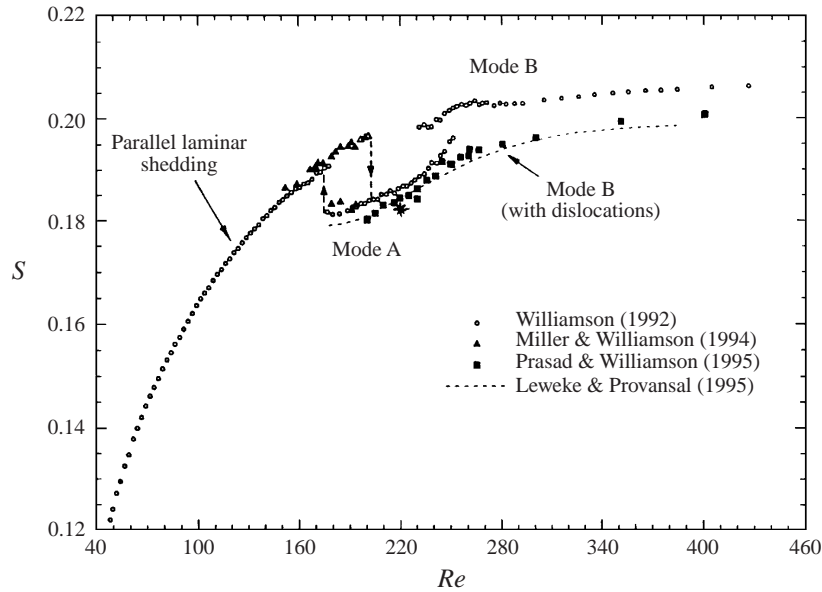
FIGURE 25. Strouhal number versus Reynolds number relation, showing lower path with dislocations. Experiments reported by Williamson (1996) (detailed in the legend); *, direct simulation by the present study.

that the two lobes are not disposed on the same horizontal line, as would be the case with just an amplitude modulation.

Therefore, by means of the analysis performed in this section, the present work clearly indicates the tendency of the flow system to have a reduction in its fundamental frequency during specific time intervals corresponding to the formation and advection of a vortex dislocation structure. This confirms the tendency shown by experimental data that a lower path of fundamental frequency variation versus Reynolds number would be followed by the system if vortex dislocations occur. In figure 25 we have plotted the mean value of the frequency reduction obtained, evaluated within the time interval given above. This value is very close to the experimental path of the curve, illustrating a global frequency decrease effect.

Having examined local variations in time and frequency domains along the span, it is interesting to provide an overview of the effect of the vortex dislocations in a space–time map. The overall time-dependent evolution of the spanwise flow structure can be seen in figure 26a where iso-v surfaces are shown as a function of z and time. So far, instantaneous images of mode A and other spanwise phenomena have been shown. This new map allows the tracking of the propagation of the spanwise structure in time. It can be seen that the propagation of the undulated spanwise structure is not homogeneous in time, but there are phase incoherences in the propagation of the fronts of mode A waves. The regions of positive and negative v velocity alternate according to the Strouhal number variations discussed previously. The topology of v contours has also mode A undulation. In a first time interval of order [945; 980], the fronts of the transverse waves evolve quasi-homothetically along the span. For time values higher than 1000, this undulation displays a slightly perturbed and 'ascending' behaviour towards higher spanwise values versus time. This is followed by the formation of the vortex dislocation and its effect on the Strouhal number, which can be shown by means of the ω_z vorticity maps (figure 26b). The
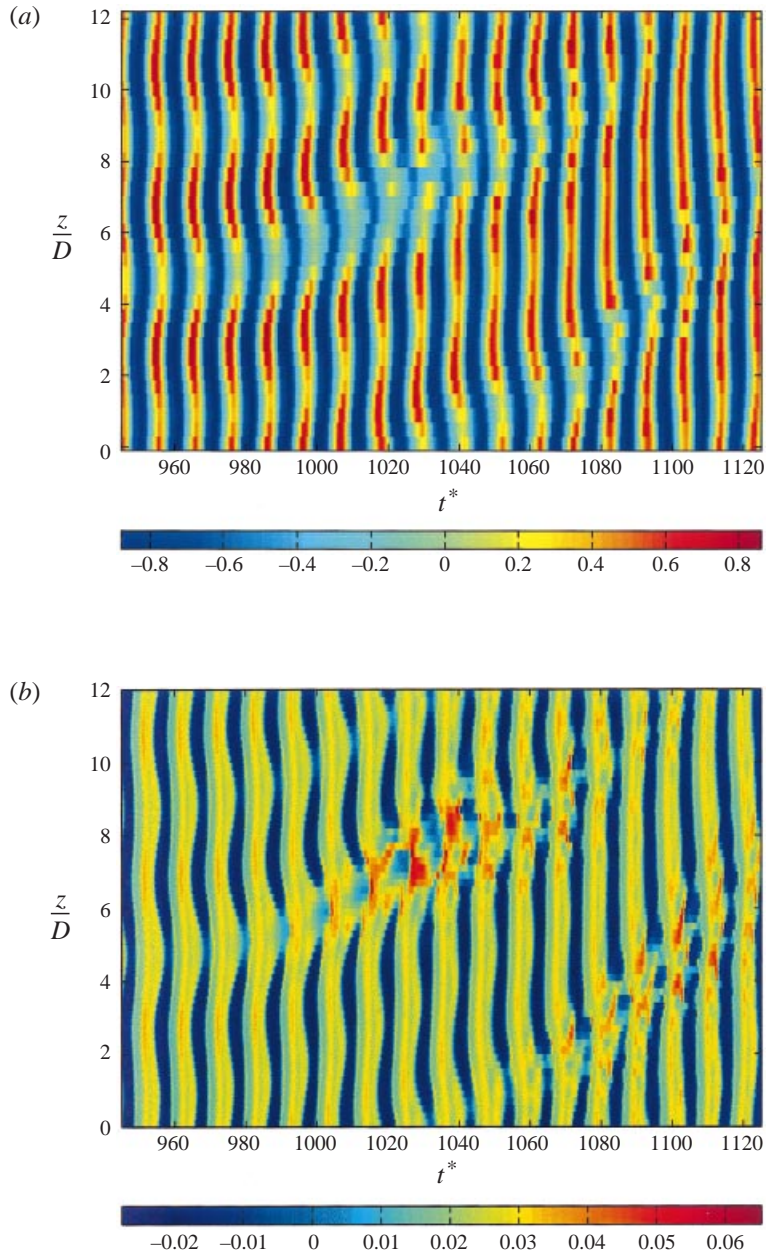
(*a*)

(*b*)

FIGURE 26. (*a*) Iso-*v* contour map and (*b*) ω_z vorticity component, on the (t, z)-plane, illustrating the perturbation fronts to mode A and their convection velocity, due to the passage of vortex dislocations. The colour scale indicates magnitudes.

decrease of the fundamental is seen in the evolution of the fronts in the interval [1050; 1070]. It is linked to the local junction that produces the 'number of events −1' in the spanwise area corresponding to the formation of a vortex dislocation (the junction occurs for instance between the seventh and eighth green vortex rows, forming the red regions in figure 26(*b*) and seen also in figure 5*d*–*f*). Below and above the area of vortex dislocation along the span, the number of events does
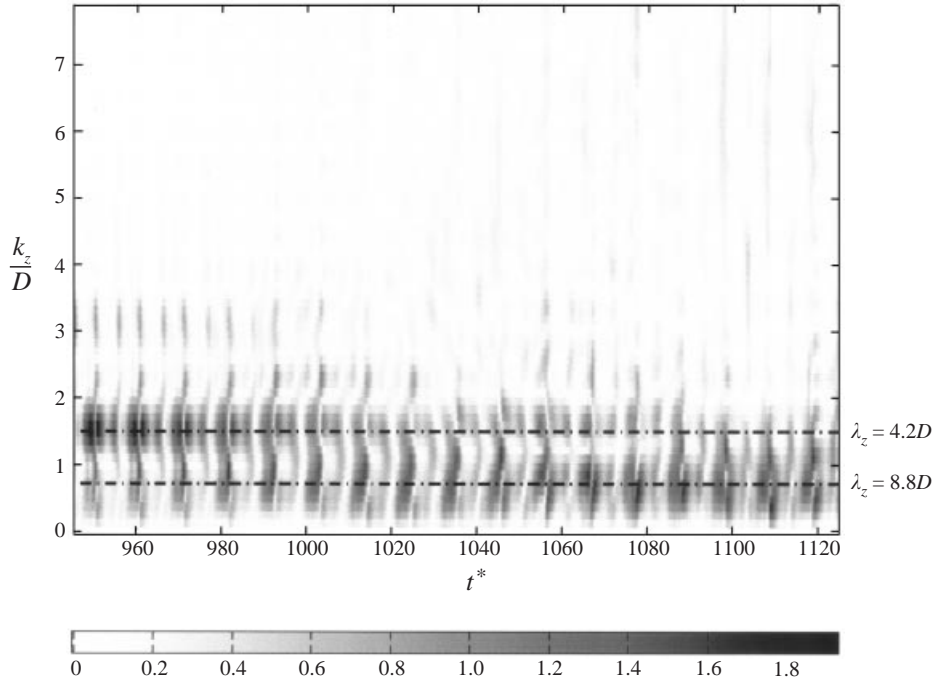
FIGURE 27. Spectral amplitude of the fundamental spatial mode on a (k_z, t)-plane: v component signals; k_z is the spatial wavenumber. The grey scale indicates magnitudes of the spectral amplitude of the fundamental.

not diminish. This is also the case in experimental visualizations by C. Williamson, personal communication (figure 14c), where the events are numbered. During the phase of the motion corresponding to the dislocation passage, the perturbation of mode A propagates quasi-linearly and the propagation velocity of this event is found to be approximately equal to 0.0509. Afterwards, mode A is again formed. The dislocation occurrence also seems to enhance the first subharmonic of wavelength $2l_z$. The quantification of the predominant wavelengths along the span is confirmed by figure 27, where the wavenumber of the fundamental is plotted versus time. The appearance of a subharmonic wavenumber is qualitatively similar to resonance phenomena appearing in an excited shear layer (Ho & Huerre 1984; Freymuth 1966), with the first subharmonic as the most energetic mode, as also predicted in that case by the linear stability theory.

4.2. *Study of spanwise mechanisms related to the appearance of natural vortex dislocations*

The above discussions concerning the dislocation structure raise the question of which effects cause the main vortex row, already undulated according to mode A, to undergo a further abrupt local change leading to vortex dislocation formation. It is reasonable to suppose that the vortex row behaves as a 'solid' body, therefore subjected mainly to pressure forces, since inviscid flow considerations are often used to analyse this kind of vortex dynamics past bluff bodies. In an attempt to find the causes of vortex dislocation, it is reasonable to examine the pressure coefficient modifications along the span. These are indeed associated with the dislocation structure formation and may be linked to pressure variations in the near-wall upstream region.
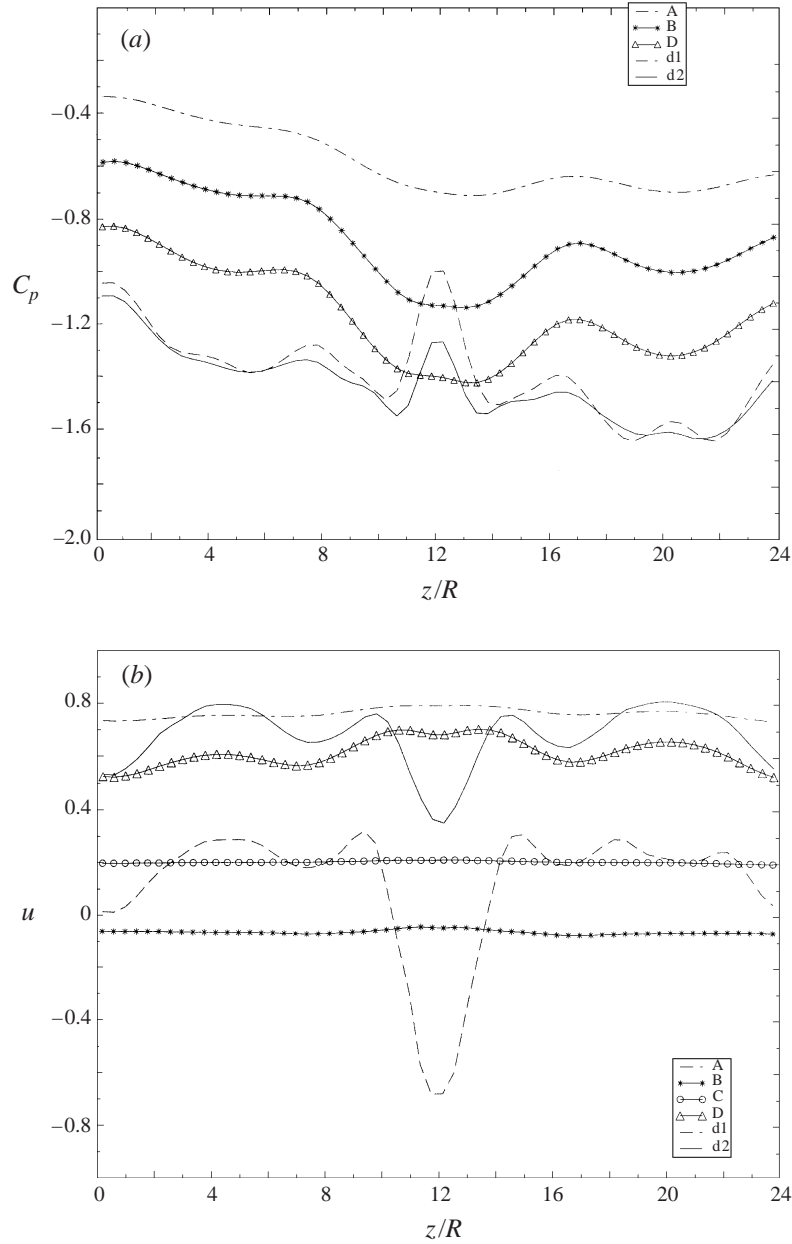
FIGURE 28. (*a*) Spanwise evolution of the pressure coefficient and (*b*) longitudinal velocity variation, at different points on the (x, y)-plane as shown in the sketch of figure 10.

Figure 28(*a*) shows the instantaneous pressure coefficient variations along the span, obtained by the present DNS and plotted at selected (x, y) coordinates as shown in the sketch and at a time value corresponding to occurrence of vortex dislocation near the half-span distance. A striking effect is the formation of a pressure increase 'bump' in the dislocation area (see variations at points d_1 and d_2; the position of points is shown in figure 10). This local pressure increase prevents the main vortex row R_1, originally non-dislocated, from advancing as fast as its neighbouring regions below and beyond
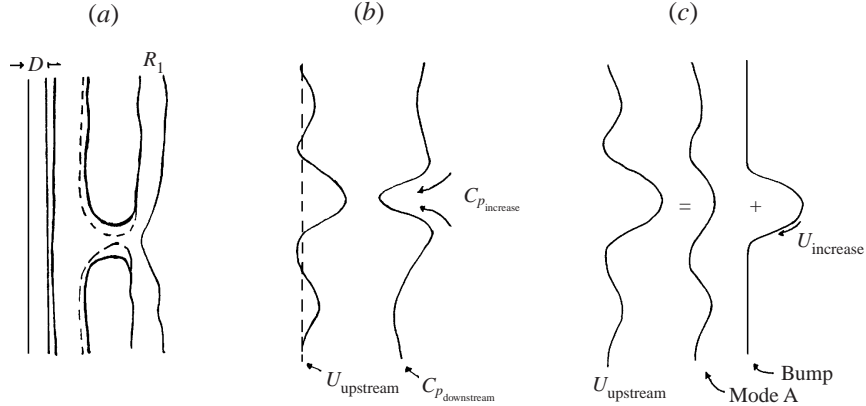
FIGURE 29. Sketch of the dislocated vortex rows: (*a*) the spanwise pressure evolution; (*b*) the upstream separation longitudinal velocity spanwise evolution and (*c*) its schematic decomposition in two parts.

the area $z/R \in [10.5; 13.5]$ (see the sketch in figure 29). It is then expected that a local discontinuity will be produced in the core of the vortex along the span in this area. Another remarkable feature occurs in the upstream separation near-wake regions of the flow, as shown for points D, B and A. An opposite-sign pressure bump is formed in the same z/R region. Under this favourable pressure gradient, the flow advances faster here. It is thus worth examining the corresponding u velocity component variations along the span in figure 28(*b*). Bump formation is again obtained, 180° out of phase compared to the pressure, as it would be expected by Bernoulli's equations. Examining the u variation at position D for instance, it is found that the central region is characterized by a distinct u velocity increase, superimposed on the undulated spanwise pattern. Therefore, the local Strouhal number of the downstream vortex shedding is expected to increase in this central area and to decrease in the immediate neighbouring spanwise locations. This difference will unavoidably create a dislocation region. This instantaneous effect is also linked to the clearly obtained time-domain frequency decrease within the specific time intervals corresponding to the passage of the vortex dislocation (quantified in §4.1). Vortex dislocations were first shown in experiments by Gaster (1969) in flows around cones. The spanwise variation of diameter, due to the form of the obstacle in this case, was responsible for the development of a change in the average frequency along the cone. In the cylinder wake, the difference in frequencies is an inherent characteristic, due to local interaction among the three velocity components (and therefore among the vorticity components). As shown in figure 16, the local production of higher r.m.s. spots of the w component along the span creates an important local variation of the u and v components, as can be deduced from the continuity equation and conservation of vorticity for the present elliptic and incompressible flow. The present DNS study shows that under the effect of the conservation mechanisms, the response of the dynamic system to all the perturbing factors to which it is subjected is a selective spanwise organization of the u distribution (that originally was uniform), according to an orderly spanwise pattern (see point D variation), causing the Strouhal number variation.

This may be schematically represented as a combination of mode A regular undulated pattern, scaling as $\cos(\beta z)$ for $z \in [0; 24R]$, plus a bump pattern modelled by a function of the form $[\cos(\beta_1 z) + \text{const}]$, for $z \in [10.5; 13.5]$ (see the sketch in figure 29). Therefore, the dislocation is a consequence of a spanwise perturbation of

the form mentioned, acting on a regularly spanwise-undulated u-velocity profile. This behaviour, in relation to the previous discussion on the secondary instability, may lead to an interesting study analysing preferred factors in the development of vortex dislocations by stability theories and by DNS. In this context, the basic two-dimensional alternating flow obtained by the Navier–Stokes simulation can be perturbed by Floquet modes, and the Floquet stability analysis can be used in conjunction with a non-uniform u velocity boundary condition along the span, reproducing the generic bump configuration, to ensure the conditions of appearance of vortex dislocations. Floquet analysis would reveal amplification of the predominant modes including the side-bands detected in the spectrum along the span by the present DNS.

5. Conclusions

The present study is a continuation of our work on analysis of three-dimensional transition in flows around bluff bodies and it focuses on understanding how three-dimensional transition features develop from nominally two-dimensional flow configurations. This study concerns Reynolds number 220, a value in a highly interesting range with respect to the development of fascinating transition phenomena. In the present work the DNS approach identifies the first stages in the three-dimensional transition, because it is able to examine the flow history from the early development of the three-dimensional mechanisms, whereas these stages evolve in very short time scales during a physical experiment. The following successive steps are determined, after a careful study of the numerical parameters and of the influence of upstream small initial disturbances applied along the span.

(i) Amplification of the w velocity component (velocity in the spanwise direction) as a function of time, whose early evolution is proven to be linear (exponential growth), before displaying nonlinear and saturation stages, accompanied by organization of the w iso-contours into distinct regular cells along the span.

(ii) Consequent amplification of streamwise vorticity, also organized along the span in quasi-periodic counter-rotating 'mushroom-like' cells.

(iii) After a substantial strengthening of this pattern, the appearance of a regular spanwise undulation (mode A), modifying the originally rectilinear, two-dimensional alternating vortex rows.

(iv) Under a bursting increase of the w-component amplitude during specific time intervals, a natural vortex dislocation starts to develop, forming a break in the 'spinal column' of the undulated von Kármán vortex rows in the near wake.

(v) The natural vortex dislocations are found to occur repetitively in the flow transition. More chaotic and quasi-periodic stages alternate as a function of time, following respectively the development and sweeping downstream of the vortex dislocations.

The appearance of the first regular undulation along the span and the corresponding wavelength are analysed in this study by the DNS approach and by an analogy to the Craik–Leibovich instability mechanism, initially conceived for studying wave-induced longitudinal-vortex instability in shear flows. The application of this theory to the three-dimensional growth of the secondary instability in the cylinder wake and the assessment of the corresponding predominant wavelength add a new element to our knowledge in the literature. A comparative discussion among this theory, the elliptic instability theory and the Floquet stability analysis is provided, on the relative benefits and limitations of each approach.

By using a rather high spanwise length ($12D$) compared to other simulations, without compromising the refinement of the grid in the (x, y)-plane over a significant distance downstream, the present study *proves the existence of vortex dislocations as an inherent feature of the flow transition* that modifies the regular spanwise undulation and has a *repetitive* and *systematic* appearance in the three-dimensional transition in the near wake. This is an original contribution of the present study that reinforces the experimental observations by Williamson (1992) on 'spot-like' natural vortex dislocations and removes controversies between other direct numerical simulations concerning the existence of this kind of structure.

By performing appropriate signal processing techniques (autoregressive modelling and wavelet analysis) the role of natural vortex dislocations in the three-dimensional transition is analysed. It has been found that the vortex dislocations occur long after the full development of the mode A pattern. They constitute a three-dimensional further modification of the von Kármán vortex rows during the three-dimensional transition. The definition of natural vortex dislocations is provided by the present study: they consist of a break of continuity in the main core of the vortex row associated with a local junction with the previously formed von Kármán vortex. This corresponds locally along the span to a (number of events $N - 1$) in respect to the shedding of vortices. This study proves that the development of these structures is associated with a *drastic fundamental frequency reduction and amplitude modulation*, quantified by the signal processing techniques. A lower path of the Strouhal–Reynolds number relationship is found to be followed by the flow system when natural vortex dislocations appear. This proves a conjecture from experimental works that the fundamental frequency tends to display a lower branch in this Reynolds number range, when vortex dislocations appear. In the present study, it is remarkable that a very good agreement with the experiments is obtained for the Strouhal number concerning the path with dislocations.

A significant result after a long time, including an order of 20 periods of the vortex shedding, is the enhancement of the first subharmonic wavelength of the spanwise undulation, as a most energetic mode. This feature can be seen as an analogy to the appearance of the first subharmonic as a predominant mode in a free shear layer, due to the occurrence of the vortex pairing phenomenon in two dimensions. In the present context, it can be conjectured that vortex dislocation formation, characterized by a local 'junction' of the main vortex row with the previous one, acts in a similar way as the vortex 'pairing' phenomenon in two dimensions, in the sense of enhancing the appearance of the subharmonic spanwise mode.

As well as the amplitude diminution along the span, it is shown that the dislocation region is characterized by areas where the pressure coefficient increases to a local maximum. The present study depicts the organization of the upstream longitudinal velocity distribution along the span as a generic bump configuration that is associated with the local Strouhal number reduction downstream, in the region of where vortex dislocations appear. This preferential shape may be used as an upstream boundary condition in future direct numerical simulation studies, to examine factors in enhancement or attenuation of vortex dislocations during the three-dimensional transition process.

Appendix. Time–frequency analysis

Time–frequency analyses were performed using continuous wavelets and autaregressive (AR) modelling. A brief review of these techniques is provided in this section.

A.1. *Wavelet analysis*

Wavelet analysis is a time-scale non-parametric tool which allows the tracking of frequency variations. A comprehensive review of wavelet transform and its application to fluid dynamics can be found in Grossman *et al.* (1985) and Farge (1992). Given the wavelet Φ, and the time series u, the wavelet transform U is defined by Flandrin (1993):

$$U(a,b) = \frac{a^{-p}}{\sqrt{C_\Phi}} \int \Phi\left(\frac{t-b}{a}\right) u(t)\mathrm{d}t \tag{A 1}$$

$$= \frac{a^{1-p}}{\sqrt{C_\Phi}} \int \hat{\Phi}^*(af)\hat{u}(f)\mathrm{e}^{2\mathrm{i}\pi fb}\mathrm{d}f \tag{A 2}$$

where a is called the scale factor and b the translation factor. Hats denote Fourier transforms, C_Φ is a real constant depending on the choice of wavelet function Φ; p is a parameter which is usually equal to $1/2$ for theoretical reasons. Since wavelet transformation is an isometry one can write the inverse transform and a Parseval-like equality:

$$u(t) = \frac{a^{p-3}}{\sqrt{C_\Phi}} \iint U(a,b)\Phi\left(\frac{t-b}{a}\right)\frac{\mathrm{d}a}{a^2}\mathrm{d}b \tag{A 3}$$

$$\int |u|^2 dt = \iint |U(a,b)|^2 \frac{\mathrm{d}a}{a^2}\mathrm{d}b = \iint S(a,b)\mathrm{d}a\mathrm{d}b \tag{A 4}$$

where $S(a,b)$ defines a real-valued time-scale density. In a time–frequency framework, these formula are usually slightly altered so that parameters a and b can be related to frequency and time. Indeed, it can be shown that for $p = 1$, $S_1 = |U(f_0/a,b)|$ may be regarded as a time–frequency density called a scalogram where f_0 is the

Resolution	$\Delta\tau$ (time units)	Δf (non-dim. freq.)
Wavelet	[46;59]	[0.015;0.019]
AR	40	10^{-4}

TABLE 1. Time and frequency uncertainties.

wavelet's central frequency in Fourier space. Roughly speaking, on a scalogram, a high-magnitude region around $(f_0/a_1, b_1)$ shows energy concentrations around time $t_1 = b_1$ at frequencies close to $f_1 = f_0/a_1$.

In this study, the Morlet wavelet was used. This wavelet is analytically defined in time or frequency domains by

$$\Phi(t) = \mathrm{e}^{2\mathrm{i}\pi f_0 t}\mathrm{e}^{-t^2/2} - \mathrm{e}^{-2\pi^2 f_0^2}\mathrm{e}^{-t^2/2}, \tag{A 5}$$

$$\hat{\Phi}(f) = \mathrm{e}^{-2\pi^2(f-f_0)} - \mathrm{e}^{-2\pi^2 f_0^2}\mathrm{e}^{-2\pi^2 f^2}. \tag{A 6}$$

The second subtracted terms on the right-hand side ensure that the Morlet wavelet has zero time mean. This condition is required for any admissible wavelet. The parameter $f_0 p$ determines the central frequency of the Morlet wavelet in Fourier space. In practical situations, f_0 is chosen to be equal or greater than 1 so that numerically, the Morlet wavelet is well approximated by

$$\Phi(t) = \mathrm{e}^{2\mathrm{i}\pi f_0 t}\mathrm{e}^{-t^2/2}, \tag{A 7}$$

$$\hat{\Phi}(f) = \mathrm{e}^{-2\pi^2(f-f_0)}. \tag{A 8}$$

f_0 must also be chosen with respect to the frequency domain of interest and the required time–frequency resolution. As a non-parametric method, the resolution of a scalogram is limited by the uncertainty relation $\Delta f \Delta\tau > k$ where Δf and $\Delta\tau$ are related to the time and frequency extent of the wavelet. The smallest value of k is obtained for Gaussian functions and depends on the way Δf and $\Delta\tau$ are defined. Possible choices for Δf and $\Delta\tau$ might respectively be the width of the modulus of the wavelet and its Fourier transform at mid-height. In that case, $k = 4\ln 2/\pi$. If $f_0 \geqslant 1$, according to equations (A 7) and (A 8), Morlet wavelets are Gaussian and hence their time–frequency resolution product is exactly equal to k. However, one must bear in mind that, due to the inherent time-scale nature of wavelet analysis, frequency and time resolutions are not constant over the time–frequency map (though their product is). On a wavelet scalogram, lower frequencies possess better frequency resolution but poorer time resolution. The situation is opposite for higher frequencies. Nevertheless, the relative frequency resolution $Q = \Delta f/f$ remains constant for a given wavelet once its various parameters (here f_0) are chosen. In this study, a central frequency f_0 between 2.0 and 2.5 leading to a relative frequency resolution Q between 0.15 and 0.19 was chosen. Therefore, the scalograms presented here have $\Delta f = fQ$ frequency and $\Delta\tau = k/(fQ)$ time uncertainties, depending on the value of the frequency f. Global frequency and time resolutions may roughly be evaluated for $f = 0.1$ which is the dominant frequency in the time series analysed. Doing so, numerical values of $0.015 \leqslant \Delta f \leqslant 0.019$ and $46 \leqslant \Delta\tau \leqslant 59$ were obtained for the present study. These values are to be compared to those of AR modelling (see table 1) which will be discussed in the next subsection.

A.2. *AR modelling*

As mentioned above, in conjunction with wavelet analysis, autoregressive (AR) analysis was also applied to convert time series into time–frequency maps. AR modelling is a widely used signal processing tool. One of its many applications is to provide high-resolution spectral descriptions of time series. It also allows a time–frequency extension which is of interest in this study.

A.2.1. *Stationary time series*

In a stationary framework, given a time series $\{u_n\}_{n \in Z}$ representing a sampled signal at rate Δt, an AR model of order N is such that

$$\sum_{k=0}^{N} a_k u_{n-k} = b_n \tag{A 9}$$

where b_n is a discrete white noise. Very few and special time series may be exactly modelled in this manner. Physically speaking, $u(t)$ should be obtained from an inertial mechanism excited by a random input. A special case of interest is the sum of n pure sine waves which follows (A 9) with $N = 2n$ and $b = 0$. In general, a finite-order AR model is only an approximation or a conceptual model where its order must be chosen high enough to enhance the quality of the approximation. For instance, modelling noisy sine waves requires an infinite-order AR model. Various algorithms allow the computation of model parameters a_n by minimizing the white noise variance σ^2. This latter gives quantitative information about how well the time series was fitted by the model. There are also several criteria which allow one to judiciously determine the order of the AR model. The most commonly used criteria are due to Akaike (1974). They are essentially based on a balance between precision and reliability since higher orders provide better model adjustment but poorer a_k estimation. The criterion used here was the cost function $Ak(N)$:

$$Ak(N) = \frac{L+N}{L-N} \sigma^2(N) \tag{A 10}$$

where L is the number of samples of the time series over which the model parameters a_k were estimated. As the model order N grows, σ^2 decreases while the ratio $(L+N)/(L-N)$ increases. Thus, this empirical criterion helps find the model order in a systematic way. Once the correct AR model is found, it is straightforward to show that the power spectral density $P(f)$ of the time series is readily given by the model parameters a_k and σ:

$$P(f) = \frac{\sigma^2}{|1 + \sum_{k}^{N} a_k e^{-2i\pi f k \Delta t}|^2}. \tag{A 11}$$

From this equation it is clear that AR models can accurately render only special spectral behaviours. For instance, there is no hope of finding $-5/3$ spectral behaviours in AR modelling data extracted from fully turbulent flows. Nevertheless, in many applications where only narrow-band or quasi-periodic behaviours are of interest, AR modelling gives fairly good results. The main advantage of AR modelling is that unlike classical non-parametric tools such as Fourier analysis, the frequency resolution is not directly limited by the time series length. If the modal parameters a_k are correctly fitted to the time series, the power spectrum is obtained with virtually infinite accuracy. Thus, high-resolution spectra may be computed for short time series. It can be shown that the frequency resolution at -3 dB (Δf_{3dB}) scales with $\gamma^{-1} N^{-2}$

for a monochromatic noisy sine wave where γ is the signal–noise ratio:

$$\Delta f_{3dB} \propto \frac{1}{\gamma N^2}. \qquad \text{(A 12)}$$

Hence with increasing γ and N, the spectral density $P(f)$ tends to an ideal zero-width Delta function. In fact, from (A 11), it can be shown that for a noisy sine wave of requency f_0, among the N complex roots of

$$x^N + \sum_{k=1}^{N} a_k x^{N-k} \qquad \text{(A 13)}$$

one pair of conjugate roots tends to $e^{\pm 2i\pi f_0 \Delta t}$. In other words, the sine wave is taken into account by a pair of complex conjugate poles of the AR model which tend to the unit circle. The AR model is supposed to behave in a similar manner in the case where several well separated Castanié (1988) harmonics are present. Harmonic components can then be extracted from pairs of poles near the unit circle. Therefore, an AR model of order $N = 2n$ is sufficient to extract n harmonics. The choice between pole or spectral density representation is dictated by the signal to noise ratio and the signal content. If γ is high enough and the time series is essentially made of pure sine waves, an AR model of order $N \geqslant 2n$ is quite sufficient. While the power spectral density $P(f)$ of such a model might not give narrow enough frequency peaks, frequency recovery from poles would be very accurate. On the other hand, for noisy and complex time series containing modulations, bursts, etc., a high-order model would be necessary. There, pole representation would not be reliable since there is no clear one-to-one relation between poles and harmonic components. However, a high enough order model ($N \gg 2n$) would entail a good power spectral density $P(f)$ with sharp and well-defined frequency peaks. From this discussion, it appears that γ is an important parameter in AR modelling. Though in almost all practical situations its value is unknown, algorithms usually provide an estimate of noise variance σ^2 which may be used to compute an approximate value of γ.

A.2.2. *Time-varying spectra*

The high-frequency resolution feature of AR models is of appreciable interest in time–frequency analysis. Namely, one models the signal over a time-limited interval or window without significant loss of frequency resolution despite the possibly short length of the window. Spectral time variations may then be tracked by moving the window along the time series and by watching the AR model parameters. The window length should be short enough to detect fast temporal changes and long enough to allow good enough signal modelling. In all cases, it should contain at least N time samples in order to uniquely define an AR model of order N. It is possible to use overlapping windows to increase the temporal rate of frequency estimations. Such a moving window AR modelling entails a time–frequency map where the time resolution is given by the length of the moving window and the frequency resolution by the model order and signal–noise ratio γ as discussed previously. Coming back to the present study, an examination of velocity and vorticity plots against time showed that frequency changes could happen over one or two periods T of the fundamental oscillation. In other words, their stationary time scale was of the order of the inverse of the Strouhal number which was about 0.1. In order to get a good model convergence, windows of length 40 time units ($\approx 4T$) were chosen. However, in order to get a closer time tracking of frequency variations, a
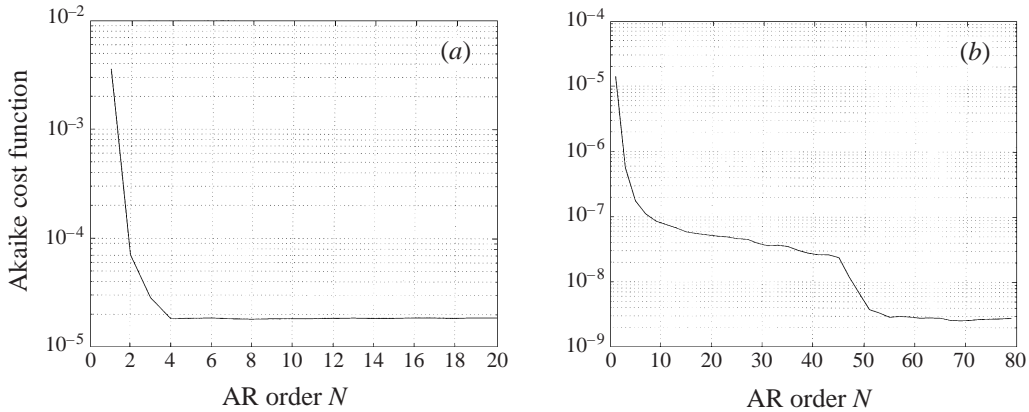
FIGURE 30. Evolution of the cost function versus the model order, for (*a*) the v velocity and (*b*) the ω_z vorticity.

50% overlap between consecutive windows was allowed. This means that frequency evaluations were updated every 20 time units (100 time samples) with windows of length 40 time units (200 time samples). This resulted in step-like time–frequency maps which were obtained through pole representation. Due to overlapping windows, each step represents a half-window and contains extra frequency information about its right-hand neighbour. This prevents abrupt frequency jumps which could, for instance, stem from non-overlapping windows of length 20 time units. Finally, the last steps on time–frequency maps are missing since their computation would have required a longer data length. Rather than computing over a half-width window or zero-padding the data to obtain a full-length window, frequency estimation over the last step was simply omitted.

Model orders were chosen with respect to Akaike's criterion (A 10). Figures 30(*a*) and 30(*b*) show the evolution of the cost function Ak versus the model order for typical windows of 200-sample long velocity and vorticity time series. As can be seen, a fourth-order model is sufficient for the velocity component v while an order of $N = 50$ is necessary for the vorticity ω_z. A close examination of v revealed indeed that only one or two harmonic components were energetically significant; v was almost noise-free and presented rather smooth amplitude and frequency modulations. Vorticity ω_z time series, on the other hand, had richer spectral content and presented sudden jumps when dislocation occurred. Therefore, they required much higher model orders. In both cases, the estimated noise power was very low and signal to noise ratios were larger than 10^3. According to (A 12), the -3 dB frequency resolution was less than 10^{-4} for v and 10^{-6} for ω_z. These very high degrees of accuracy should not conceal the fact that (A 12) does not rigorously apply when several harmonics are present. As a matter of fact, the task of predicting frequency resolution of such models is not an easy one. While the subject remains controversial (Duvaut 1994), empirical results are often applied. Here, an accuracy of 10^{-4} seemed a reasonable value for both v and ω_z time series. These values along with those of wavelet scalograms are collected in table 1.

REFERENCES

AKAIKE, A. 1974 A new look at the statistical model identification. *IEEE Trans. Autom. Control* A1 **19**, 716–723.

ALLAIN, J., BRAZA, M., FAGHANI, D. & PERSILLON, H. 1999 The role of natural vortex dislocations in

the transition to turbulence of the flow past a circular cylinder by DNS. In *Proc. Symp. on Direct and Large Eddy Simulations, Isaac Newton Institute for Mathematical Sciences, Cambridge, May 12–14* (ed. P. R. Voke, N. D. Sandham & L. Kleiser), pp. 191–222. Kluwer.

AMSDEN, A. A. & HARLOW, F. H. 1970 The SMAC method: A numerical technique for calculating incompressible fluid flows. *Tech. Rep.* LA-4370. Los Alamos Scientific Laboratory.

ANDREWS, D. G. & MCINTYRE, M. E. 1978a An exact theory of nonlinear waves on a lagrangian-mean flow. *J. Fluid Mech.* **89**, 609–646.

ANDREWS, D. G. & MCINTYRE, M. E. 1978b On wave-action and its relatives. *J. Fluid Mech.* **89**, 647–664.

BARKLEY, D. & HENDERSON, R. 1996 Three-dimensional floquet stability analysis of the wake of a circular cylinder. *J. Fluid Mech.* **322**, 215–241.

BAYLY, B. J. 1986 3-dimensional instability of elliptic flow. *Phys. Rev. Lett.* **57**, 2160.

BLOOR, M. S. 1964 Transition to turbulence in the wake of a circular cylinder. *J. Fluid Mech.* **19**, 290–304.

BOUHADJI, L. & BRAZA, M. 1999 Direct numerical simulation of transonic flows around a wing. In *Proc. Symp. on Direct and Large Eddy Simulations, Isaac Newton Institute for Mathematical Sciences, Cambridge, May 12–14* (ed. P. R. Voke, N. D. Sandham & L. Kleiser), pp. 359–369. Kluwer.

BRAZA, M., CHASSAING, P. & HA MINH, H. 1986 Numerical study and physical analysis of the pressure and velocity fields in the near wake of a circular cylinder. *J. Fluid Mech.* **165**, 79–130.

BROWAND, F. K. & TROUTT, T. R. 1980 A note on the spanwise structure in the two-dimensional mixing layer. *J. Fluid Mech.* **97**, 771–781.

BROWAND, F. K. & TROUTT, T. R. 1985 The turbulent mixing layer: Geometry of large vortices. *J. Fluid Mech.* **158**, 489–509.

CASTANIÉ, F. 1988 *Traitement Du Signal*. Institut National Polytechnique de Toulouse, France.

CRAIK, A. D. D. 1982a The generalized lagrangian-mean equations and hydrodynamic stability. *J. Fluid Mech.* **12**, 27–35.

CRAIK, A. D. D. 1982b Wave-induced longitudinal-vortex instability in shear flows. *J. Fluid Mech.* **125**, 37–52.

DOUGLAS, J. 1962 Alternating direction methods for three-space variables. *Numerische Mathematik* **4**, 41–63.

DUVAUT, P. 1994 *Traitement Du Signal*. Paris: Hermes.

FARGE, M. 1992 Wavelet transforms and their applications to turbulence. *Ann. Rev. Fluid Mech.* **24**, 395–457.

FLANDRIN, P. 1993 *Temps-Fréquence*. Paris: Hermes.

FREYMUTH, P. 1966 On transition in a separated laminar boundary layer. *J. Fluid Mech.* **25**, 683–704.

GASTER, M. 1969 Vortex shedding from slender cones at low reynolds numbers. *J. Fluid Mech.* **38**, 565–576.

GONG, W. M., TAYLOR, P. A. & DÖRNBRACK, A. 1996 Turbulent boundary layer flow over fixed aerodynamically rough two-dimensional sinusoidal waves. *J. Fluid Mech.* **312**, 1–37.

GOUJON-DURAND, S., JENFFER, P. & WESFREID, J. E. 1994 Downstream evolution of the Bénard-von Karman instability. *Phys. Rev. Lett.* **50**, 308–313.

GROSSMAN, A., MORLET, J. & PAUL, T. 1985 Integral transforms associated to square integrable representations. *J. Math. Phys.* **27**, 2473–2479.

HENDERSON, R. D. 1997 Nonlinear dynamics and pattern formation in turbulent wake transition. *J. Fluid Mech.* **352**, 65–112.

HO, C. M. & HUERRE, P. 1984 Perturbed free shear layers. *Ann. Rev. Fluid Mech.* **16**, 365–424.

HOARAU, Y., RODES, P., BRAZA, M. & ANNE-ARCHARD, D. 2000 Direct numerical simulation of three-dimensional transition in the incompressible flow around a wing. *Fourth EUROMECH Fluid Mech. Conf., Eindhoven, The Netherlands, November 19–23.*

JACKSON, P. S. 1973 The flow round obstacles in boundary layers. PhD thesis, University of Cambridge.

JESPERSON, D. C. & LEVIT, D. 1991 Numerical simulation of flow past a tapered cylinder. *AIAA Paper* 91-0751.

JIN, G. & BRAZA, M. 1987 A non-reflecting outlet boundary condition for incompresible unsteady Navier–Stokes calculations. *J. Comput. Phys.* **107**, 239–253.

LANDMAN, M. J. & SAFFMAN, P. G. 1987 The three-dimensionnal instability of strained vortices in viscous fluid. *Phys. Fluids* **30**, 2339–2342.

LASHERAS, J. C. & MEIBURG, E. 1990 Three-dimensional vorticity modes in the wake of a flat plate. *Phys. Fluids* A **2**, 371–380.

LESIEUR, M., COMTE, P. & MÉTAIS, O. 1995 Numerical simulation of coherent vortices in turbulence. *Appl. Mech. Rev.* **48** (3), 121–149.

LEWEKE, T. & WILLIAMSON, C. H. K. 1998 Three-dimensional instabilities in wake transition. *Eur. J. Mech.* B *Fluids* **17**, 571–586.

MITTAL, R. & BALACHANDAR, S. 1995 Effect of three-dimensionality of the lift and drag of nominally two-dimensional cylinders. *Phys. Fluids* **7**, 1841–1865.

PERSILLON, H. & BRAZA, M. 1998*a* Direct numerical simulation of three-dimensional vortex dynamics in the unsteady flow past a circular cylinder. *Proc. 4th ECCOMAS Computational Fluid Dynamics Conference, September.*

PERSILLON, H. & BRAZA, M. 1998*b* Physical analysis of the transition to turbulence in the wake of a circular cylinder by three-dimensional Navier–Stokes simulation. *J. Fluid Mech.* **365**, 23–89.

PERSILLON, H., BRAZA, M. & JIN, G. 1995 Prediction of transition features in the flow past a circular cylinder in three dimensions. In *Proc. 5th ISOPE: Intl Offshore Mech. and Polar Engng Conf, The Hague, The Netherlands, June 11–16* (ed. J. S. Chung, J. Warderier & H. Maeda). Intl Soc. Offshore and Polar Engrs.

PERSILLON, H., BRAZA, M. & WILLIAMSON, C. 1997 Three-dimensional coherent structures in the flow around a circular cylinder by direct numerical simulation. In *Simulation and Identification of Organised Structures in Flows, IUTAM Symp., Lyngby, Denmark, May 25–28* (ed. I. Sorensen, E. Hopfinger & N. Aubry). Kluwer.

PHILLIPS, W. R. C., WU, Z. & LUMLEY, J. L. 1996 On the formation of longitudinal vortices in a turbulent boundary layer over wavy terrain. *J. Fluid Mech.* **326**, 321–341.

ROSHKO, A. 1954 On the drag and shedding frequency of two-dimensional bluff bodies. *NACA TN* 3169.

SADEH, W. & BRAUER, H. 1980 A visual investigation of turbulence in stagnation flow about a circular cylinder. *J. Fluid Mech.* **99**, 53–64.

THOMPSON, M., HOURIGAN, K. & SHERIDAN, J. 1994 Three-dimensional instabilities in the cylinder wake. *Intl Colloq. on Jets, Wakes and Shear Layers, Melbourne, Australia, April 18–20* (ed. I. Shepherd & K. Hourigan), paper 10. CSIRO.

VINCENDEAU, E. 1995 Analyse conditionnelle et estimation stochastique appliquées à l'étude des structures cohérentes dans la couche de mélange. PhD thesis, Université de Poitiers.

WALEFFE, F. 1992 On the three-dimensional instability of strained vortices. *Phys. Fluids* A **2**, 76–80.

WILLIAMSON, C. H. K. 1992 The natural and forced formation of spot-like vortex dislocations in the transition of a wake. *J. Fluid Mech.* **243**, 393–441.

WILLIAMSON, C. H. K. 1996 Vortex dynamics in the cylinder wake. *Ann. Rev. Fluid Mech.* **24**, 477–539.

ZHANG, H., FEY, U., NOAK, B. R. & ECKELMANN, H. 1996 On the transition of the circular cylinder. *Phys. Fluids* **7**, 779–794.